applied sciences

MDPI

Article

Statistical Ensemble Modelling of Dynamic Hysteresis Loops in Single-Domain and Non-Interacting Magnetic Nanoparticles by Using a Double-Well Rate Equation Approach

Nikolaos Maniotis [1,*], Ioanna Kranioti [2], Nikolaos Vordos [2] and Michael Maragakis [2]

[1] Department of Physics, Aristotle University of Thessaloniki, 54124 Thessaloniki, Greece
[2] Department of Physics, Democritus University of Thrace, 69100 Kavala, Greece; iokrani@physics.duth.gr (I.K.); nvordos@physics.duth.gr (N.V.); mmara@physics.duth.gr (M.M.)
* Correspondence: nimaniot@physics.auth.gr

Featured Application

This work presents a computational framework based on a double-well rate-equation model for predicting dynamic hysteresis in single-domain ferromagnetic nanoparticles under alternating magnetic fields. The model is particularly relevant for magnetic hyperthermia applications, where accurate estimation of hysteresis losses and specific loss power (SLP) is essential for optimizing nanoparticle design and therapeutic efficiency. By incorporating realistic distributions of particle size, magnetic anisotropy, and easy-axis orientation within a statistical ensemble approach, the method enables rapid and physically transparent prediction of heating performance in experimentally relevant nanoparticle systems. The developed framework provides a computationally efficient alternative to micromagnetic simulations and can be directly applied to the design and optimization of magnetic nanoparticle-based hyperthermia agents.

Abstract

Magnetic hyperthermia relies on the ability of magnetic nanoparticles (MNPs) to dissipate heat under alternating magnetic fields, with the heating efficiency commonly quantified through the specific loss power (SLP). Accurate estimation of SLP requires realistic modeling of the dynamic magnetic response of nanoparticle ensembles, particularly in the ferromagnetic single-domain regime where hysteresis losses dominate. In the present work, we developed a computational framework in Mathematica based on the thermally activated Stoner–Wohlfarth model to simulate dynamic hysteresis loops and estimate SLP in ensembles of non-interacting magnetic nanoparticles. The model incorporates experimentally relevant distributions of particle diameter, magnetic anisotropy, and easy-axis orientation, enabling realistic representation of nanoparticle polydispersity and orientation disorder. Thermal activation was introduced through Arrhenius-type Néel switching probabilities, while the dynamic magnetization evolution was obtained numerically through solution of the corresponding rate equations. The framework was tested for magnetite nanoparticles, one of the most widely used materials in magnetic hyperthermia, considering typical single-domain ferromagnetic particle sizes in the range of 15–30 nm and effective anisotropy K_{eff} values representative, 3 kJ/m^3 < K_{eff} < 20 kJ/m^3 of experimentally reported systems. Simulations were performed under clinically relevant alternating magnetic fields with amplitudes up to 24 kA/m and frequencies ranging from 100 to 765 kHz. The model successfully reproduced dynamic hysteresis loop evolution and enabled systematic investigation of the influence of nanoparticle size, anisotropy, and orientation distributions on loop shape, symmetry, and SLP. The developed code provides a computationally accessible

Check for updates

Academic Editor: Marco Rossi

Received: 1 June 2026
Revised: 16 June 2026
Accepted: 18 June 2026
Published: 26 June 2026

Correction Statement: This article has been republished with a minor change. The change does not affect the scientific content of the article and further details are available within the backmatter of the website version of this article.

Copyright: © 2026 by the authors. Licensee MDPI, Basel, Switzerland. This article is an open access article distributed under the terms and conditions of the Creative Commons Attribution (CC BY) license.

tool for researchers working in magnetic hyperthermia, allowing direct connection between microscopic nanoparticle properties and macroscopic heating performance. By enabling parametric mapping of dynamic hysteresis behavior and SLP dependence, the framework may support the rational optimization of magnetic nanoparticle systems for biomedical hyperthermia applications.

Keywords: magnetic nanoparticles; dynamic hysteresis loop; statistical ensemble modelling; double well system; rate equations; stochastic Stoner–Wohlfarth model

1. Introduction

Magnetic nanoparticles (MNPs) have attracted considerable scientific interest during the last decades due to their unique magnetic properties and their broad range of technological and biomedical applications, including magnetic recording, spintronics, magnetic sensing, targeted drug delivery, and magnetic hyperthermia [1–7]. In magnetic hyperthermia, magnetic nanoparticles are subjected to alternating magnetic fields, converting electromagnetic energy into heat through irreversible magnetic losses [8,9]. The heating efficiency strongly depends on the dynamic magnetization processes occurring at the nanoscale and therefore requires accurate theoretical modeling of magnetic hysteresis under time-dependent magnetic fields [10–12].

Several theoretical and computational approaches have been developed to describe the magnetization dynamics of magnetic nanoparticles. Micromagnetic simulations based on the Landau–Lifshitz–Gilbert (LLG) equation constitute one of the most widely used numerical techniques for describing magnetization reversal processes [13–16]. Such methods, implemented in software packages such as OOMMF and MuMax3, solve the nonlinear vectorial dynamics of the magnetization by accounting for effective magnetic fields, damping mechanisms, exchange interactions, and anisotropy effects [17–19]. Although these methods provide detailed information regarding magnetization dynamics at the nanoscale, they become computationally demanding when large ensembles of nanoparticles are considered, particularly under experimentally realistic conditions relevant to magnetic hyperthermia [7,20].

In practical hyperthermia experiments, even a small amount of magnetic material contains an enormous number of nanoparticles [21]. For example, one milligram of magnetite nanoparticles with diameters in the range of 15–25 nm may contain more than 10^{13} particles. Modeling such systems using direct LLG simulations is computationally prohibitive, since only a limited number of particles can be simulated explicitly [22]. Furthermore, realistic nanoparticle ensembles exhibit significant distributions in particle size, magnetic anisotropy, and easy-axis orientation, all of which strongly influence the resulting hysteresis losses and heating efficiency [14,23–26]. Consequently, numerical micromagnetic approaches often require substantial simplifications regarding particle number, geometry, or statistical variability.

An alternative approach consists of describing the magnetic nanoparticle as a thermally activated bistable system. For single-domain ferromagnetic nanoparticles, the magnetic energy landscape can be represented by a double-well potential derived from the Stoner–Wohlfarth model [27,28]. The two minima correspond to metastable magnetization states separated by an energy barrier whose height depends on the magnetic anisotropy, particle volume, applied magnetic field, and the orientation of the easy axis. Thermal fluctuations induce transitions between these states, and the time evolution of the occupation proba-

bilities can be described by a system of rate equations based on Néel–Brown transition theory [29,30].

The double-well formulation offers several important advantages [31,32]. First, it provides a direct connection between the underlying energy landscape and the observed magnetization dynamics. The energy barriers, transition rates, and occupation probabilities retain clear physical meaning, allowing a transparent interpretation of magnetization reversal mechanisms. Second, the model naturally incorporates thermal activation effects, which are essential for describing nanoparticle behavior at room temperature and under hyperthermia conditions. Third, the computational cost is several orders of magnitude lower than that associated with solving the nonlinear Landau–Lifshitz–Gilbert equation, making ensemble calculations feasible even when considering millions or billions of statistically distinct nanoparticles.

The present work develops and compares two implementations of the double-well rate-equation framework. The first implementation considers an idealized ensemble of identical nanoparticles with perfectly aligned easy axes and no statistical distributions. This oriented-particle model serves as a reference system and allows direct comparison with classical Stoner–Wohlfarth predictions. By eliminating sources of statistical variability, it provides insight into the intrinsic influence of thermal activation and dynamic field effects on the shape and area of the hysteresis loop.

The second implementation extends the model toward experimentally realistic nanoparticle ensembles by introducing a full statistical description of particle properties. In this case, the magnetization dynamics are averaged over distributions of particle diameter, magnetic anisotropy constant, and easy-axis orientation. The angle between the external magnetic field and the anisotropy axis is explicitly included in the energy landscape and transition-rate calculations. Consequently, the ensemble magnetization is obtained through statistical averaging over a multidimensional parameter space that reflects the intrinsic heterogeneity of real nanoparticle samples.

The incorporation of particle-size distributions is particularly important because the magnetic energy barrier scales with particle volume, leading to exponential variations in relaxation times and switching probabilities [33]. Similarly, variations in magnetic anisotropy produce broad distributions of energy barriers even for particles of identical size. Easy-axis orientation distributions further modify the effective switching fields and magnetization reversal mechanisms predicted by the Stoner–Wohlfarth theory. The combined effect of these distributions can significantly alter the dynamic hysteresis loop, often producing behavior that cannot be reproduced using a single representative particle characterized by average parameter values.

A major strength of the statistical ensemble formulation developed in this work is that it preserves the microscopic physics of individual nanoparticles while simultaneously capturing the macroscopic response of experimentally relevant systems. Rather than approximating an ensemble by a hypothetical average particle, the model calculates the magnetization contribution of each statistically weighted nanoparticle population and subsequently performs ensemble averaging. This approach accurately accounts for the highly nonlinear dependence of energy barriers and transition rates on particle size and anisotropy, avoiding the inaccuracies associated with mean-value approximations.

Compared with other approaches commonly employed to model magnetic nanoparticle dynamics, the present statistical ensemble double-well rate-equation framework offers a favorable balance between physical realism and computational efficiency. Linear response theory (LRT)-based models are computationally simple and provide accurate predictions in the superparamagnetic regime under low field amplitudes, but their assumption of a linear relationship between magnetization and applied field limits their applicability when

significant hysteresis and nonlinear magnetization reversal occur [34–36]. Static and quasi-static Stoner–Wohlfarth (SW) models accurately describe coherent rotation and switching of single-domain particles but neglect thermal activation and dynamic effects, making them less suitable for predicting frequency-dependent hysteresis losses under alternating magnetic fields [37,38]. At the opposite end of the modeling spectrum, numerical kinetic Monte Carlo and Langevin dynamics simulations can explicitly account for stochastic thermal fluctuations and time-dependent magnetization processes, but often require substantial computational resources, particularly when realistic nanoparticle ensembles with broad distributions of size, anisotropy, and orientation are considered [11,20,32]. The double-well rate-equation approach employed in this work retains the essential physics of thermally activated magnetization reversal through Néel–Brown transition rates while remaining computationally efficient enough to model large statistical ensembles representative of experimental hyperthermia systems. Consequently, it provides an attractive intermediate framework that bridges the gap between oversimplified analytical descriptions and computationally intensive numerical simulations.

The proposed methodology therefore bridges the gap between analytical theories and large-scale nanoparticle ensembles. It combines the physical rigor of the Stoner–Wohlfarth energy landscape, the thermal activation framework of Néel–Brown theory, and the statistical description of realistic nanoparticle populations within a computationally efficient model. As a result, it enables systematic investigations of dynamic hysteresis loops under conditions directly relevant to magnetic hyperthermia while maintaining a level of computational efficiency that is unattainable with conventional micromagnetic simulations.

The primary objective of this work is to establish a comprehensive statistical-ensemble framework for predicting the dynamic hysteresis behavior of single-domain ferromagnetic nanoparticles under alternating magnetic fields and to quantify the influence of particle-size, anisotropy, and orientation distributions on the resulting magnetic response and energy dissipation.

2. Materials and Methods

2.1. Theoretical Framework

The dynamic magnetic response of single-domain ferromagnetic nanoparticles subjected to an alternating magnetic field was investigated using a stochastic double-well model derived from the Stoner–Wohlfarth theory of coherent magnetization reversal. The approach assumes that each nanoparticle behaves as a single magnetic domain possessing uniaxial magnetic anisotropy and undergoing thermally activated transitions between two metastable magnetization states. The model was implemented in Wolfram Mathematica [39] and was developed in two stages. First, an idealized system of identical and perfectly oriented nanoparticles was considered in order to establish a reference case. Subsequently, the model was extended to a statistical ensemble framework incorporating experimentally relevant distributions of particle diameter, magnetic anisotropy, and easy-axis orientation. The calculations were performed under conditions relevant to magnetic hyperthermia, where nanoparticles are subjected to sinusoidal magnetic fields of the form $H = H_0 \sin(2\pi f t)$, where H_0 and f are the field amplitude and frequency respectively.

2.2. Stoner–Wohlfarth Energy Landscape

The magnetic energy of a nanoparticle with uniaxial anisotropy was described by

$$E(\theta, \varphi) = K_{eff} V sin^2(\theta) - \mu_0 M_s V H \cos(\theta - \varphi) \quad (1)$$

with θ the angle between the easy axis and the magnetic moment μ and φ the angle between the "easy" axis and the magnetic field H [40]. Moreover, K_{eff} is the effective anisotropy constant, V is the magnetic core volume and Ms is the saturation magnetization. The first term represents the energy contribution due to the effective anisotropy of the nanoparticle while the second term, known as Zeeman energy, is proportional to nanoparticle's energy originating by the interaction with the sinusoidal magnetic field. For each value of the applied magnetic field, the energy landscape exhibits two local minima corresponding to metastable magnetization states and a saddle point separating them. Within the double-well approximation, magnetization reversal occurs through thermally activated transitions between these minima. Three characteristic angles were therefore considered:

- θ_1: first metastable minimum;
- θ_2: second metastable minimum;
- θ_3: saddle-point maximum.

The energy barriers associated with thermally activated switching were calculated as

$$E_+ = E(\theta_3) - E(\theta_1) \text{ and } E_- = E(\theta_3) - E(\theta_2)$$

where E_+ and E_- represent the forward and reverse activation energies, respectively.

2.3. Thermally Activated Néel Switching

Thermal fluctuations were incorporated through an Arrhenius-type description of Néel relaxation. The transition rates between the two magnetic states were calculated according to

$$n_+ = n_0 \exp(-E_+/k_BT) \quad (2)$$

$$n_- = n_0 \exp(-E_-/k_BT) \quad (3)$$

where n_0 denotes the attempt or Larmor frequency set equal to 10^9 Hz, k_B is Boltzmann's constant, and T is the absolute temperature.

2.4. Rate Equation Formalism and Magnetization Calculation

The dynamic magnetization response of the ensemble was described by a master-equation approach in which the time evolution of magnetization results from the competition between forward and reverse thermally activated transitions [41,42]. Calling P_1 the occupation probability of position $E(\theta_1)$ and P_2 the corresponding one of position $E(\theta_2)$, the time evolution of P_1 is estimated by:

$$\frac{\partial P_1}{\partial t} = P_2 n_- - P_1 n_+ = (1 - P_1) n_- - P_1 n_+ \quad (4)$$

Considering $\partial/\partial t = (\partial/\partial H)(\partial H/\partial t)$ and $M = M_s(P_1 cos\theta_1 + (1 - P_1) cos\theta_2)$ Equation (4) becomes:

$$\frac{\partial M}{\partial H} = \frac{M_s(cos\theta_1 - cos\theta_2)\left[n_- - \left(\frac{n_+ + n_-}{cos\theta_1 - cos\theta_2}\right)\left(\frac{M}{M_s} - cos\theta_2\right)\right]}{\frac{\partial H}{\partial t}} \quad (5)$$

where a time dependent applied magnetic field $H(t)$ of frequency f with a sweeping rate $\frac{\partial H}{\partial t} = \pm 4 f H_0$ is assumed. For negative sweeping rates, the magnetic field reversal occurs (demagnetization process).

The resulting differential equation was solved numerically using Mathematica's ND-Solve routine. Separate integrations were performed for the virgin magnetization curve, the ascending branch of the hysteresis loop, and the descending branch, allowing recon-

struction of the complete dynamic hysteresis cycle. Within the numerical implementation, the magnetic field was introduced as a continuously varying quantity and the switching probabilities were recalculated at each integration step. This procedure enabled simulation of dynamic hysteresis loops beyond the quasi-static approximation and allowed investigation of frequency-dependent magnetic losses. The time-dependent master equation was numerically integrated using the NDSolve function available in Wolfram Mathematica. This routine employs adaptive numerical integration methods with automatic step-size control and stiffness detection to accurately solve ordinary differential equations. In the present work, NDSolve was used to calculate the temporal evolution of the occupation probability $p_1(t)$ under the sinusoidal magnetic field $H(t) = H_{\max}\cos(\omega t)$. The integration was performed over multiple field cycles until a periodic steady-state solution was achieved. To eliminate transient effects associated with the initial conditions, only the final stabilized cycle was retained for the calculation of magnetization, dynamic hysteresis loops, hysteresis area, and specific loss power.

2.5. Dynamic Hysteresis Loop Reconstruction and SLP Estimation

The magnetization solutions obtained from the numerical integration of the rate equations were combined to reconstruct the complete dynamic hysteresis loop M(H). Loop symmetry and continuity were used as numerical consistency criteria. Since the model describes non-interacting nanoparticle ensembles under symmetric field excitation, physically realistic solutions are expected to satisfy $M(H) = -M(-H)$ (and obviously regarding the coercive field Hc: $|-\mathrm{Hc}| = \mathrm{Hc}$) within numerical accuracy. The resulting hysteresis loops provide direct information regarding coercivity, remanence, switching dynamics, and magnetic losses. Numerical solutions of Equation (5) based on multiple demagnetization ($\frac{\partial H}{\partial t} = -4fH_0$) and magnetization ($\frac{\partial H}{\partial t} = +4fH_0$) cycles provide the full hysteresis loop for specific values of the involved parameters ($K_{eff}, V, M_s, H_0, f, T$).

The energy dissipated per magnetic cycle was obtained from the area enclosed by the dynamic hysteresis loop:

$$\mathrm{A} = \oint \mathrm{M}\,\mathrm{dH} \tag{6}$$

The specific loss power was then calculated as SLP = $f \times$ A. Since the hysteresis area directly reflects the energy converted into heat during each field cycle, the calculated SLP provides a quantitative measure of magnetic hyperthermia performance.

2.6. Utilization of Statistical Distributions at the Ensemble Level

To account for experimentally observed nanoparticle polydispersity, particle diameters D were represented through a lognormal distribution:

$$\mathrm{P(D)} = 1/(\mathrm{D}\sigma_{\mathrm{D}}\sqrt{(2\pi)})\,\exp[-(\ln(\mathrm{D}) - \mu_{\mathrm{d}})^2/(2\sigma\mathrm{D}^2)] \tag{7}$$

where μ_{D} and σ_{D} correspond to the distribution parameters. The average particle volume was calculated from $\langle \mathrm{V} \rangle = \int_0^\infty \left(\pi D^3/6\right) P(D)\, dD$ and subsequently introduced into the magnetic energy expression (1). This approach enables incorporation of realistic size distributions while maintaining computational efficiency.

Variations in magnetic anisotropy arising from particle shape, crystal defects, surface effects, and structural heterogeneity were incorporated through a probability density function P(K). The effective anisotropy contribution was obtained through statistical averaging $\langle \mathrm{K} \rangle = \int_0^\infty K\, P(K)\, dK$ where either Gaussian or lognormal distributions can be employed depending on the characteristics of the experimental system. The anisotropy distribution introduces a realistic spread of energy barriers and switching probabilities within the nanoparticle ensemble.

The relative orientation between the applied magnetic field and the nanoparticle easy axis strongly influences the magnetic energy landscape. To account for orientation disorder, a normalized truncated Gaussian distribution was introduced:

$$P(\varphi) = \exp[-(\varphi - \varphi_0)^2/(2{\sigma_\varphi}^2)] / \int_0^\pi exp\left[-(u - \varphi_0)^2/\left(2\sigma_\varphi^2\right)\right] du \quad (8)$$

where φ_0 denotes the central orientation and σ_φ characterizes the angular dispersion.

The orientational averaging entering the Zeeman term was calculated numerically according to

$$\langle \cos(\theta - \varphi) \rangle = \int_0^\pi cos(\theta - \varphi)\ P(\varphi)\ d\varphi \quad (9)$$

This formulation enables simulation of random powders, partially aligned nanoparticle systems, and anisotropic particle assemblies frequently encountered in biomedical ferrofluids.

For systems with distributed nanoparticle properties, ensemble averaging was performed after computing the full time-dependent magnetization for each parameter realization. The macroscopic magnetization was obtained as a weighted integral over the distributions of particle size, anisotropy, and easy-axis orientation. Importantly, average material parameters were not substituted directly into the nonlinear dynamical equations, since the magnetization dynamics depend nonlinearly on these quantities through the energy barrier and transition rates.

2.7. Model Assumptions and Scope

The present framework assumes non-interacting single-domain nanoparticles and neglects explicit dipolar and exchange interactions. This approximation is consistent with the classical Stoner–Wohlfarth formalism and is further justified by both experimental and theoretical observations indicating that strong dipolar coupling generally reduces hysteresis loop area and consequently decreases heating efficiency [43–48]. The model therefore represents nanoparticle systems in which inter-particle interactions are minimized through surface coatings, steric stabilization, or low particle concentrations, conditions commonly pursued in magnetic hyperthermia applications. The developed computational framework is intended as a predictive and exploratory tool for investigating the influence of nanoparticle properties on dynamic hysteresis behavior and SLP. By linking experimentally accessible material parameters with hyperthermia performance, the code provides a practical platform for nanoparticle optimization and for the interpretation of experimental magnetic hyperthermia measurements.

In addition to the physical assumptions described above, hysteresis loop symmetry was employed as a practical validation criterion for the numerical solutions. During the simulations, the particle size, anisotropy, and orientation distribution parameters were systematically varied until numerically stable and physically consistent solutions were obtained. Convergence of the differential equation toward a symmetric hysteresis loop was considered an indication that the selected ensemble parameters produced a self-consistent description of the nanoparticle system within the thermally activated Stoner–Wohlfarth framework. This procedure also provides a useful inverse-modeling strategy for identifying realistic combinations of magnetic parameters from experimentally observed hysteresis behavior. The framework was designed to provide computationally efficient predictions of dynamic hysteresis behavior in large nanoparticle ensembles while retaining the essential physical mechanisms governing thermally activated magnetization reversal.

The Wolfram Mathematica codes developed for the implementation of the double-well rate-equation model, including both the oriented-particle framework and the statistical ensemble formulation incorporating size, anisotropy, and easy-axis orientation distributions,

are publicly available in a GitHub repository. The repository contains the complete source code, example input parameters, and documentation required to reproduce the calculations presented in this work. The repository URL is provided in the Data Availability Statement.

3. Results

3.1. Dynamic Hysteresis of Oriented Nanoparticles Without Statistical Distributions

Initially, the double-well rate-equation model was applied to ensembles of identical single-domain nanoparticles with perfectly aligned easy axes ($\phi = 0$). This idealized configuration was used as a reference system in order to investigate the individual effects of anisotropy, particle size, excitation frequency, and temperature on dynamic hysteresis behavior. Ordered systems of MNPs have also been utilized in previous studies due to their unique properties and enhancing thermal effects in magnetic hyperthermia [9,26,49–51]. Except in the case of varied frequency, all the SLP values were calculated at the maximum frequency used (765 kHz). In addition, all the loops, except the varied temperature case study, were simulated at room temperature (300 K).

3.1.1. Effect of Effective Anisotropy

Figure 1 presents the calculated hysteresis loops for 15 nm nanoparticles under an alternating magnetic field of amplitude 24 kA/m (0.03 T) for different values of the effective anisotropy constant K_{eff}. The corresponding magnetic characteristics such as remanence magetiztion Mr, the coercive field Hc and the loop area are summarized in Table 1 together with the SLP calculation.

Table 1. Characteristic values of a hysteresis loop (Mr, Ms, Hc, A, SPL) obtained for the various effective anisotropy values.

Keff (J/m^3)	5000	6000	7000	10,000	12,000	13,000	15,000	16,000
Mr (Am^2/kg)	4.872	7.340	10.973	29.777	45.908	52.991	63.643	67.198
Ms (Am^2/kg)	75.468	75.470	75.472	75.472	75.465	75.467	75.459	75.307
Hc (T)	0.00038	0.00056	0.000891	0.002855	0.00551	0.00732	0.0118	0.0143
Area (J/kg)	0.0916	0.228	0.668	1.534	2.043	2.794	4.284	4.953
SLP (W/gr)	70.1	174.5	510.9	1173.2	1562.5	2137.5	3277.4	3789.0

A pronounced increase in hysteresis loop area was observed with increasing anisotropy. The remanent magnetization increased from approximately 4.9 Am^2/kg at $K_{eff} = 5000$ J/m^3 to more than 67 Am^2/kg at $K_{eff} = 16,000$ J/m^3, while the coercive field Hc increased by nearly two orders of magnitude. The observed increase in coercivity with increasing anisotropy reflects the larger energy barriers opposing magnetization reversal. Nevertheless, coercivity is a multifactorial property and should not be considered a direct measure of anisotropy in general, since it may also be affected by particle size, temperature, magnetic interactions, and orientation effects. Simultaneously, the hysteresis area increased from 0.092 J/kg to 4.95 J/kg and the predicted specific loss power increased from approximately 70 W/g to almost 3800 W/g. The behavoir of SLP with effective anisotropy is depicted in Figure 2.

These results demonstrate the strong influence of anisotropy on thermally activated magnetization reversal. Larger anisotropy values produce higher energy barriers, reducing thermally induced switching and leading to larger hysteresis losses. Consequently, the heating efficiency increases substantially as the anisotropy approaches values for which the magnetic field can still induce reversal while maintaining significant irreversibility.

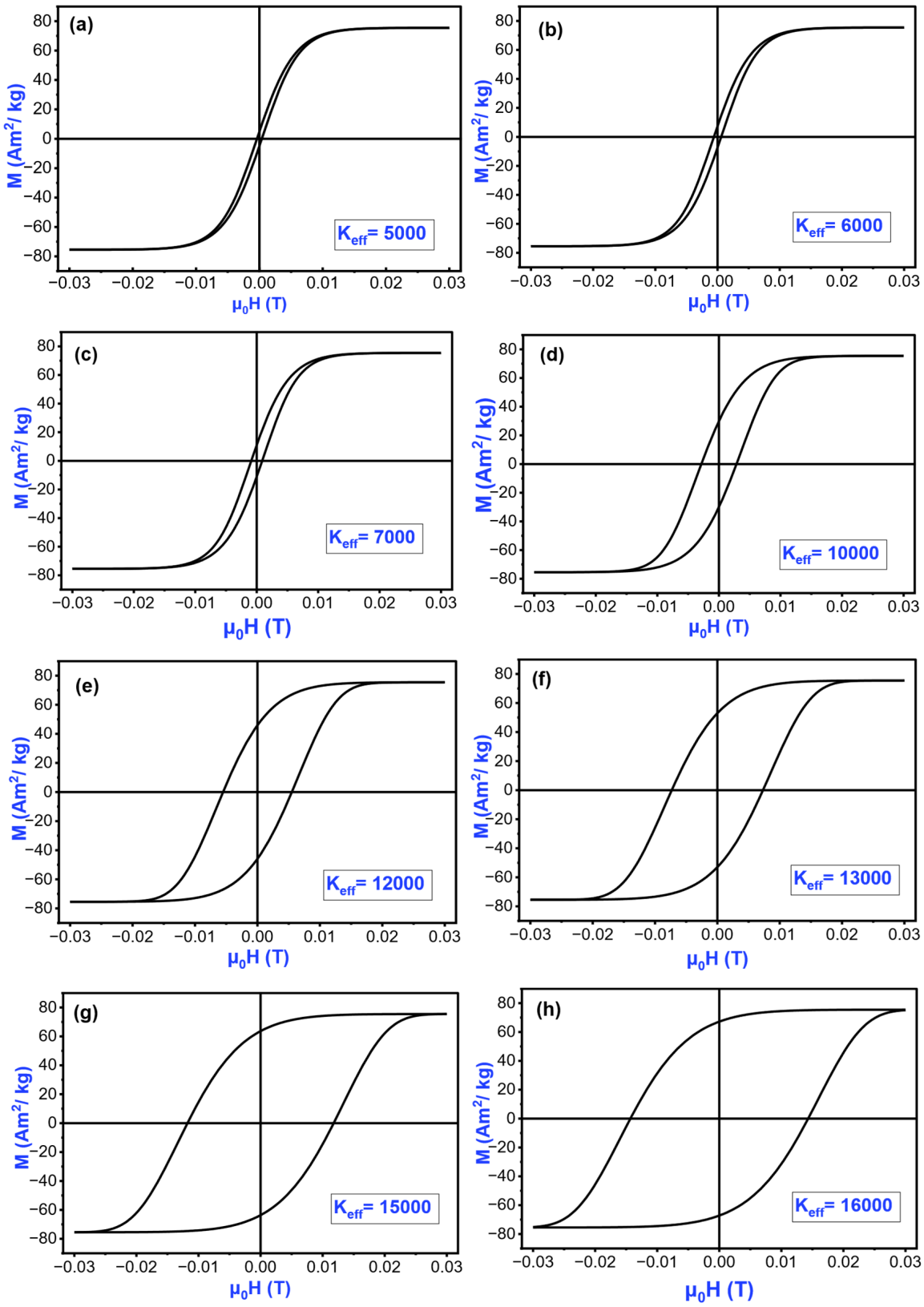


Figure 1. (**a**–**h**) Plots for 15 nm nanoparticle size at different anisotropy values. The K_{eff} values are given in J/m^3 at the inset of each figure.

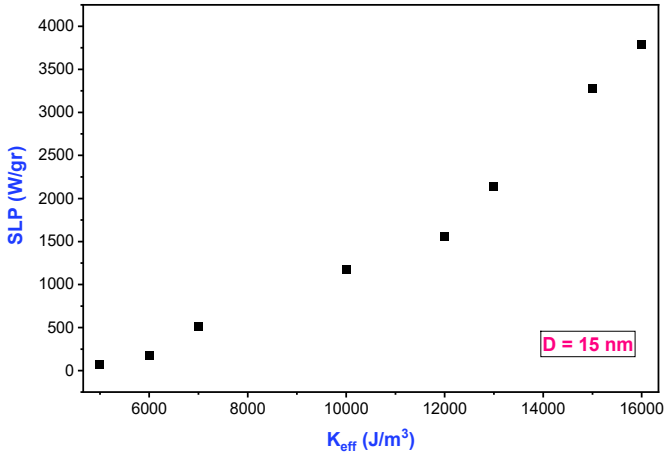


Figure 2. SLP as a function of anisotropy for 15 nm MNPs system without statistical distributions in size, effective anisotropy and orientation angle.

3.1.2. Effect of Particle Diameter

The influence of particle size was investigated by varying the diameter while keeping the anisotropy constant at $K_{eff} = 7000\ \mathrm{J/m^3}$. The resulting hysteresis loops are shown in Figure 3 while the hysteresis parameters are summarized in Table 2.

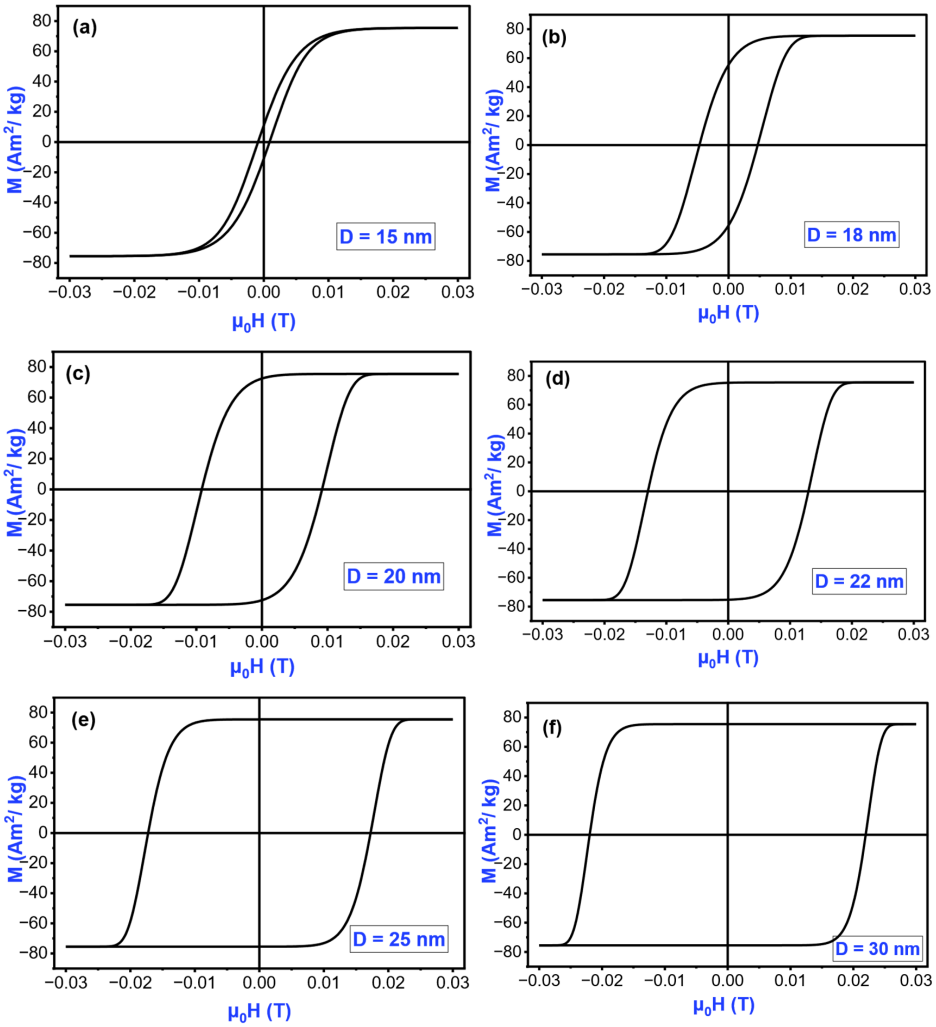


Figure 3. Dynamic hysteresis loops plots for an anisotropy value of K_{eff} = 7000 J/m^3 at different nanoparticle diameter values namely (**a**) 15 nm, (**b**) 18 nm, (**c**) 20 nm, (**d**) 22 nm, (**e**) 25 nm and (**f**) 30 nm.

Table 2. Hysteresis loop characteristics at various diameters and sizes for a constant anisotropy K_{eff} = 7000 J/m^3.

D (nm)	15 nm	18 nm	20 nm	22 nm	25 nm	30 nm
Mr (Am^2/kg)	10.971	55.414	72.464	75.239	75.470	75.472
Ms (Am^2/kg)	75.463	75.471	75.468	75.476	75.472	75.472
Hc (T)	0.00089	0.00467	0.00917	0.01298	0.01724	0.02200
Area (J/kg)	0.494	1.622	3.052	3.991	5.134	6.560
SLP (W/gr)	377.84	1240.74	2334.86	3053.04	3927.52	5020

An increase in diameter led to a dramatic increase in remanence, coercivity, hysteresis area, and SLP. The hysteresis area increased from approximately 0.49 J/kg for 15 nm particles to 6.56 J/kg for 30 nm particles, while the predicted SLP increased from approximately 378 W/g to over 5000 W/g. This behavior originates from the cubic dependence of the energy barrier on particdiameter: $\Delta E \propto KV \propto KD^3$.

It is obvious that from the above results that as the particle volume increases, the thermal stability of the magnetization increases significantly, resulting in broader hysteresis loops and enhanced energy dissipation. The strong SLP—size dependence is depicted in Figure 4 and highlights the importance of precise particle-size control in magnetic hyperthermia applications. It should be emphasized that the nanoparticles considered in this study have diameters between 15 and 30 nm, a size range that is typically associated with single-domain magnetite nanoparticles. Consequently, the magnetization reversal process does not involve magnetic domain-wall nucleation or propagation. Instead, each nanoparticle behaves as a single magnetic entity whose dynamics are governed by thermally activated transitions between metastable states. Therefore, the observed increase in hysteresis area and specific loss power with particle size originates from the volume dependence of the anisotropy energy barrier ($\Delta E \propto KV$), rather than from domain-related effects. As the particle diameter increases, the magnetic volume and corresponding energy barrier increase, leading to enhanced hysteresis losses and greater heat generation under alternating magnetic fields.

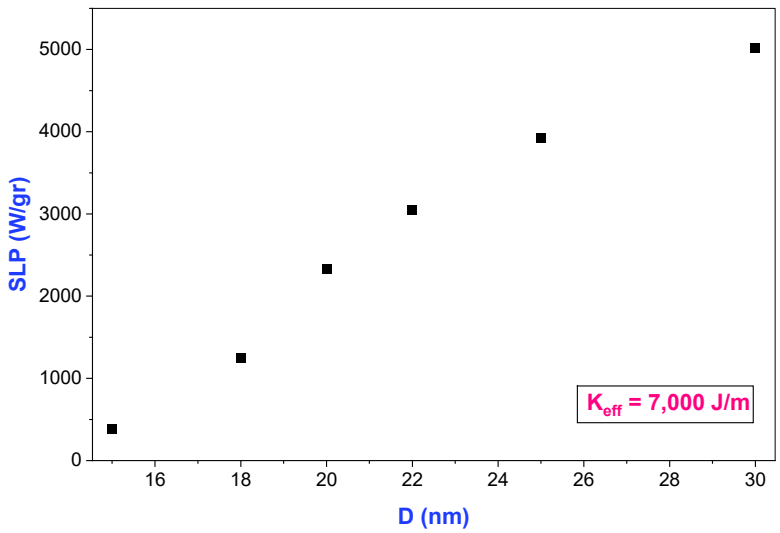


Figure 4. Specific power loss as a function of MNPs diameter for K_{eff} = 7000 J/m^3.

3.1.3. Effect of Excitation Frequency

The influence of frequency on dynamic hysteresis loop was investigated for nanoparticles with $K_{eff} = 10,000$ J/m^3 and diameter 18 nm. The results are presented in Figure 5 and Table 3.

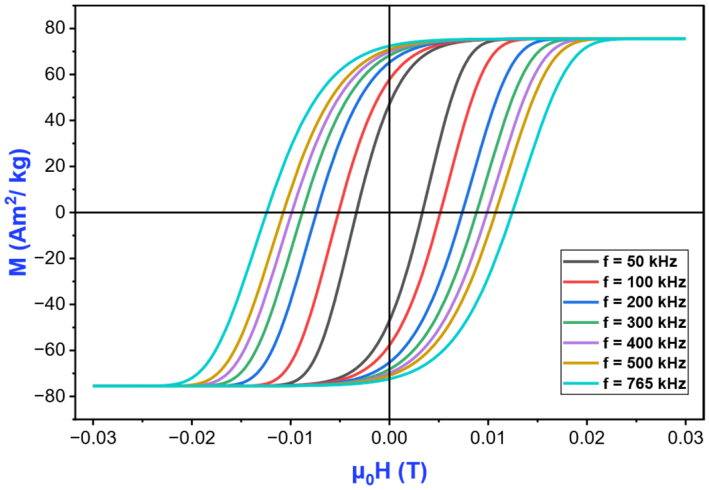


Figure 5. Magnetic hysteresis loops for different values of frequency for an anisotropy of $K_{eff} = 10,000\ \mathrm{J/m^3}$ and MNPs diameter of D = 18 nm.

Table 3. Characteristic values of the hysteresis loops as a function of frequency for a nanoparticle diameter of D = 18 nm and anisotropy $K_{eff} = 10,000\ \mathrm{J/m^3}$.

Frequency (KHz)	50	100	200	300	400	500	765
Mr (Am^2/kg)	47.100	57.758	65.237	68.244	69.876	70.904	72.395
Ms (Am^2/kg)	75.472	75.472	75.472	75.472	75.472	75.472	75.472
Hc (T)	0.003	0.005	0.007	0.009	0.010	0.011	0.012
Area (J/kg)	0.902	1.431	2.082	2.507	2.825	3.080	3.585
SLP (W/gr)	45.123	143.071	416.327	752.070	1129.825	1539.818	2742.837

Increasing the excitation frequency from 50 kHz to 765 kHz resulted in systematic increases in remanence, coercivity, hysteresis area, and SLP. The hysteresis area increased from approximately 0.90 J/kg to 3.59 J/kg, while SLP increased from approximately 45 W/g to more than 2700 W/g. The observed behavior reflects the dynamic nature of the magnetization reversal process. At higher frequencies, the characteristic timescale of the applied field becomes comparable to or shorter than the thermal relaxation time of the nanoparticles. Consequently, the magnetization cannot fully follow the field, leading to larger phase lags and increased hysteresis losses. The frequency effect on SLP is depicted in Figure 6.

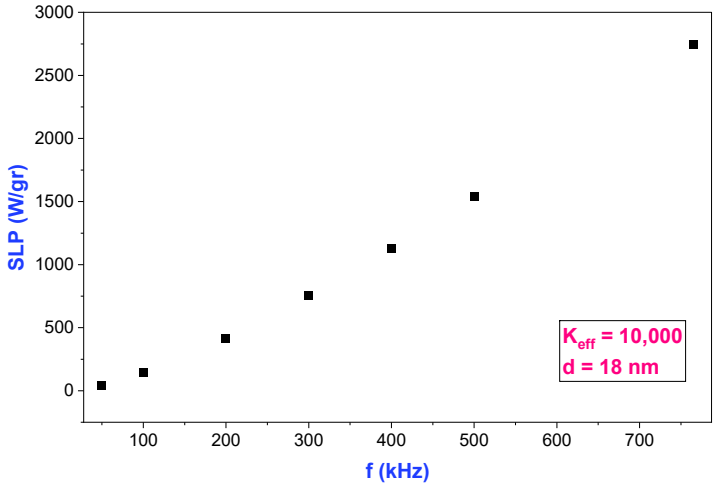


Figure 6. Specific power loss as a function of frequency for $K_{eff} = 10,000\ \mathrm{J/m^3}$ and MNPs with diameter of 18 nm.

3.1.4. Effect of Temperature

The effect of temperature was evaluated for nanoparticles with $K_{eff} = 10,000$ J/m^3 and diameter 18 nm. Figure 7 and Table 4 summarize the obtained results.

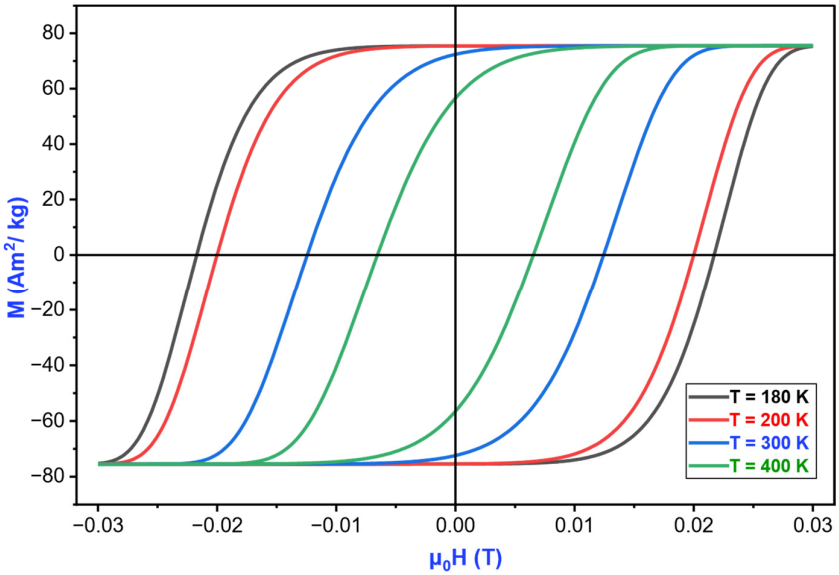


Figure 7. Magnetic hysteresis loops for different values of temperature for of $K_{eff} = 10,000$ J/m^3 and a nanoparticle diameter of D = 18 nm.

Table 4. Characteristic values of the hysteresis loop as a function of temperature for a nanoparticle diameter of D = 18 nm and $K_{eff} = 10,000$ J/m^3.

T (K)	180	200	300	400
Mr (Am^2/kg)	75.45693	75.41589	72.3953	56.5329
Ms (Am^2/kg)	75.4717	75.4717	75.4717	75.4717
Hc (T)	0.021711	0.02	0.01244	0.00655
Area (J/kg)	6.419165	5.895409	3.58541	1.82258
SLP (W/gr)	4910.661	4509.988	2742.84	1394.27

As temperature increased from 180 K to 400 K, a substantial reduction in remanence, coercivity, hysteresis area, and SLP was observed. The hysteresis area decreased from approximately 6.42 J/kg at 180 K to 1.82 J/kg at 400 K, corresponding to a reduction of nearly 72%. Similarly, SLP decreased from approximately 4911 W/g to 1394 W/g. This trend can be attributed to the enhancement of thermal fluctuations. As temperature increases, thermal activation facilitates transitions between the two energy wells, reducing magnetic irreversibility and consequently decreasing hysteresis losses. The effect on SLP is also graphically illustrated in Figure 8.

The observed decrease in coercivity with increasing temperature can be attributed to enhanced thermal activation of the magnetic moments. Within the Néel–Brown framework, the probability of a transition between the two metastable states is governed by an Arrhenius-type relation, $f_{ij} = f_0 \exp(-\Delta E_{ij}/k_B T)$. As temperature increases, the ratio $\Delta E_{ij}/k_B T$ decreases, resulting in a higher probability of thermally activated magnetization reversal. Consequently, the magnetic moments require a smaller externally applied field to overcome the effective energy barrier, leading to a reduction in the coercive field. In physical terms, thermal fluctuations assist the reversal process and reduce the magnetic irreversibility of the system at a measurement time τ_m. This effect becomes increasingly pronounced as the thermal energy approaches the anisotropy energy barrier, producing

narrower hysteresis loops with lower coercivity and reduced hysteresis losses. The aforementioned behavior is connected directly to the classical expression for the temperature dependence of coercivity in single-domain particles [52]:

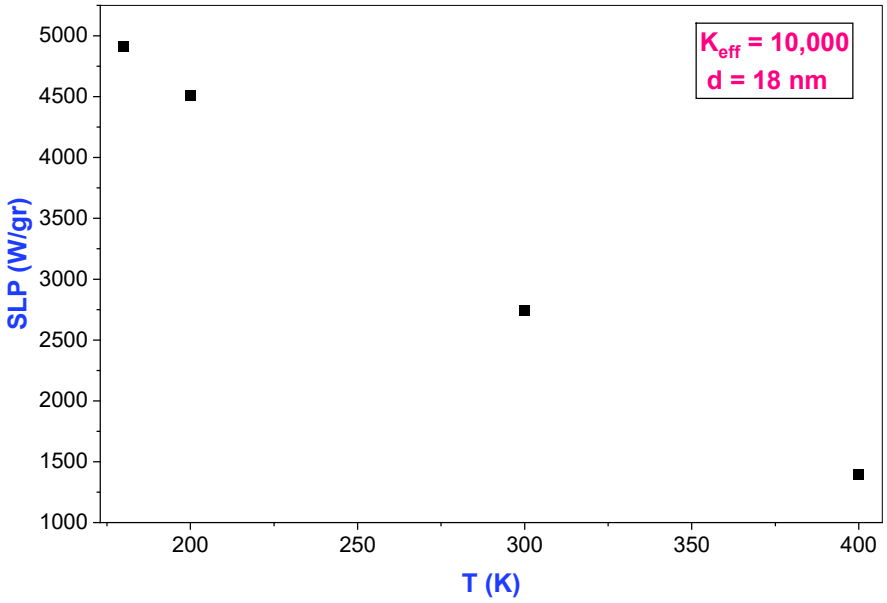


Figure 8. SLP dependence with temperature for $K_{eff} = 10,000$ J/m^3 and D = 18 nm.

$$H_c(T) \approx H_c(0)\left[1 - \left(\frac{k_B T}{KeffV}\ln\frac{\tau_m}{\tau_0}\right)^{1/2}\right] \quad (10)$$

which explicitly shows that H_c decreases as T increases because thermal fluctuations lower the effective barrier for magnetization reversal.

3.2. Statistical Ensemble Model Including Property Distributions

The previous results correspond to idealized nanoparticle systems characterized by identical particle properties. However, experimentally synthesized nanoparticles exhibit distributions in anisotropy, particle size, and easy-axis orientation. Therefore, the double-well model was extended to a statistical ensemble formulation incorporating these distributions. All the hysteresis loop graphs and SLP values are calculated at the maximum frequency used (765 kHz) and at room temperature (300 K). When it is not denoted the distributions are taken for size, anisotropy and angle φ standard deviations that are equal to $\sigma_D = 0.25$, $\sigma_K = 0.3$ and $\sigma_\varphi = \pi/72$ respectively.

3.2.1. Effect of Anisotropy Distribution

The influence of anisotropy dispersion was investigated through the standard deviation σ_K while maintaining a mean anisotropy of 7000 J/m^3, a mean particle diameter of 15 nm and a mean orientation angle of 30°. The obtained hysteresis loops for the various effective anisotropy deviations are shown in Figure 9.

Increasing σ_K from 0.1 to 0.7 resulted in systematic increases in remanence, coercivity, hysteresis area, and SLP. The hysteresis area increased from 0.509 J/kg to 1.187 J/kg, while SLP increased from approximately 389 W/g to 908 W/g. All the hysteresis parameters are shown in Table 5. We notice that a distribution of anisotropy constants leads to very significant changes both in the remanence magnetization and in the coercivity. In Figure 9 we see that the irreversibility grows with σK while the saturation magnetization is not significantly affected. The shape of the loops is not only affected by the increase in irreversibility with increasing σK but the loop goes from being more vertical for the system of

nearly identical MNPs in terms of K_{eff} ($\sigma K/\langle K_{eff}\rangle = 0.1$) to being tilted due to a decrease in susceptibility. Meanwhile, the enclosed area is increased. When the MNPs are saturated the magnetization dispersion, which is maximum around the coercive field, drops again and becomes zero. This makes sense if we consider that, when saturated, the MNPs no longer see an energy barrier proportional to Keff since they energetically are at the only minimum left at that field. As we are dealing with non-interacting MNP systems, we can correctly think in its distribution of coercive fields. These results show that, although the mean value of the distribution remains unchanged for different σK (i.e., all the Ms values are the same), the dispersion of coercivity and remanence is increased with σK, which is reflected in the hysteresis area under the magnetization dispersion curves.

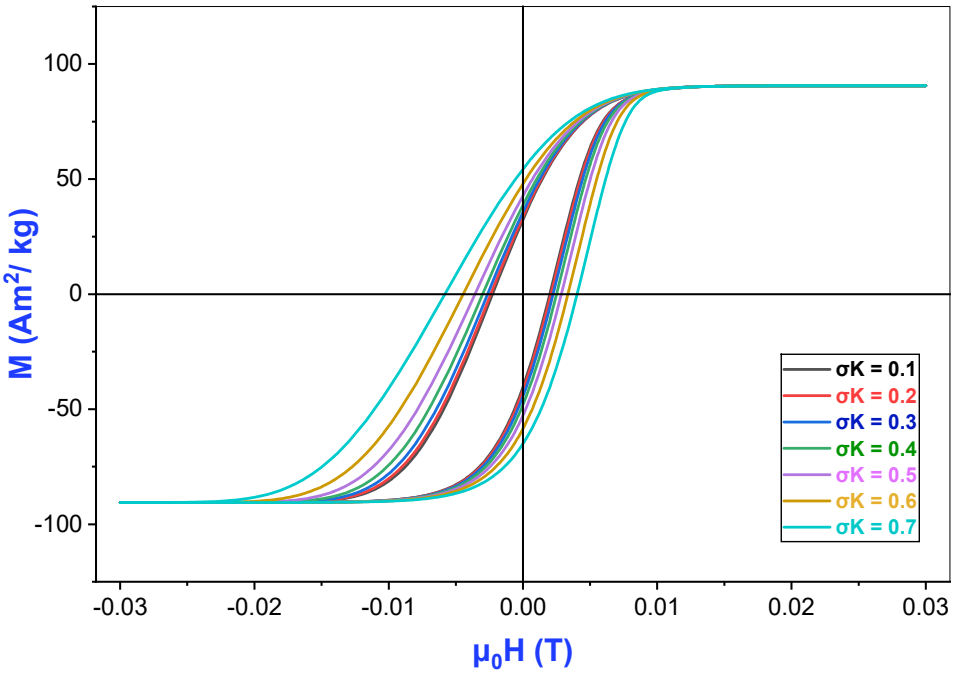


Figure 9. Magnetic hysteresis loops for different values of the standard deviation of anisotropy.

Table 5. Characteristic values of the hysteresis loop as a function of the standard deviation of anisotropy for 15 nm diameter nanoparticles with mean $K_{eff} = 7000\ \mathrm{J/m^3}$.

σK	0.1	0.2	0.3	0.4	0.5	0.6	0.7
Mr (Am^2/kg)	36.346	37.739	40.029	43.310	47.695	53.194	59.591
Ms (Am^2/kg)	90.559	90.559	90.559	90.575	90.561	90.561	90.561
Hc (T)	2.14×10^{-3}	2.24×10^{-3}	2.44×10^{-3}	2.75×10^{-3}	3.23×10^{-3}	3.90×10^{-3}	4.93×10^{-3}
Area (J/kg)	0.509	0.531	0.544	0.643	0.696	0.932	1.187
SLP (W/gr)	389.06	405.95	415.94	491.57	532.56	713.09	907.95

The increase in heating efficiency indicates that anisotropy dispersion introduces nanoparticle populations with larger energy barriers, which contribute disproportionately to irreversible magnetization reversal. This finding highlights the importance of considering anisotropy distributions when predicting hyperthermia performance. The SLP increase with σK is aslo depicted in Figure 10.

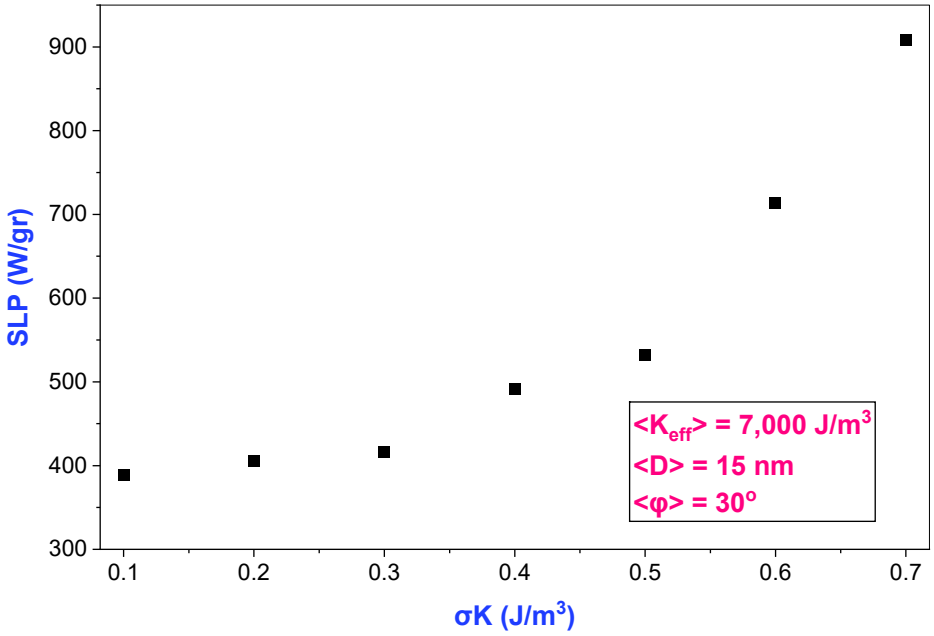


Figure 10. SLP dependence on anisotropy standar deviation for the MNPs system under study (mean anisotropy of 7000 J/m^3, mean particle diameter of 15 nm and a mean orientation angle of 30°).

3.2.2. Effect of Particle Size Distribution

The influence of size dispersion was examined for the same MNPs system, presented in Section 3.2.1 (mean anisotropy of 7000 J/m^3, mean particle diameter of 15 nm and a mean orientation angle of 30°), through different values of the diameter standard deviation σ_D. The results are presented in the corresponding hysteresis loops of Figure 11 and summary Table 6.

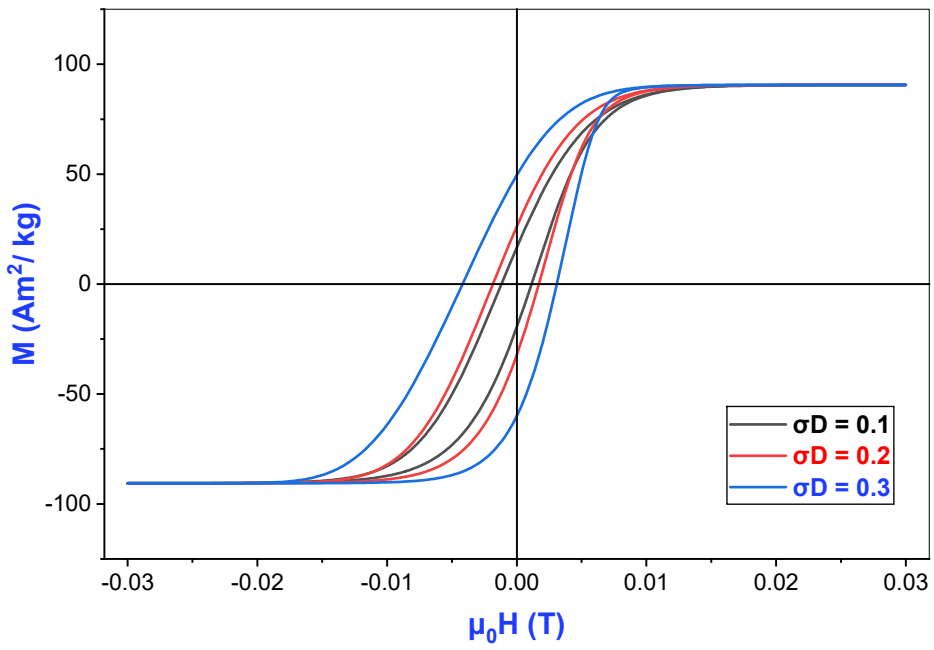


Figure 11. Magnetic hysteresis loops for different values of the standard deviation of nanoparticle diameter for a mean diameter of 15 nm and mean effective anisotropy 7000 J/m^3.

Table 6. Characteristic values of the hysteresis loop as a function of the standard deviation of nanoparticle diameter for 15 nm particles with $K_{eff} = 7000$ J/m^3.

σD	0.1	0.2	0.3
Mr (Am^2/kg)	17.980	29.156	54.721
Ms (Am^2/kg)	90.567	90.577	90.566
Hc (T)	0.00149	0.00176	0.00363
Area (J/kg)	0.2549	0.3379	1.3013
SLP (W/gr)	194.964	258.460	995.463

Increasing the width of the size distribution led to substantial increases in coercivity, hysteresis area, and SLP. For example, increasing σ_D from 0.1 to 0.3 increased the hysteresis area from 0.255 J/kg to 1.30 J/kg, while SLP increased from approximately 195 W/g to nearly 1000 W/g. The effect is considerably stronger than expected from a mean-particle approximation because the energy barrier depends on particle volume (D^3). Consequently, a relatively small fraction of larger nanoparticles contributes significantly to the total energy dissipation.

3.2.3. Effect of Easy-Axis Orientation

To investigate the influence of the angle ϕ between the easy axis and the applied magnetic field, calculations were performed for nanoparticles with diameters of 15 nm and 20 nm, dimensions that are commonly employed in magnetic hyperthermia applications. For each orientation angle (10–40°), the value of the effective anisotropy constant K_{eff} was adjusted in order to obtain hysteresis loops exhibiting the highest degree of symmetry. The dynamic hysteresis loops are shown in Figures 12 and 13 while the resulting values are summarized in the corresponding Tables 6 and 7 for 15 and 20 nm respectively.

Table 7. Hysteresis parameters extracted from Figure 12 together with the results that correspond to the loop calculated without distributions and for 15 nm oriented magnetic nanoparticles.

φ (Degrees)	0	0	10	20	30	40	45
Keff (J/m^3)	**9000 Without Distributions**	**9000**	**8000**	**7500**	**7000**	**5000**	**3500**
Mr (Am^2/kg)	22.106	55.977	55.583	43.012	36.043	15.436	6.115
Ms (Am^2/kg)	90.566	90.566	90.566	90.566	90.566	90.566	90.566
Hc (T)	1.31×10^{-3}	3.61×10^{-3}	3.65×10^{-3}	2.50×10^{-3}	2.11×10^{-3}	8.63×10^{-3}	3.61×10^{-3}
Area (J/kg)	0.5	1.16	1.173	0.8	0.7	0.3	0.1
SLP (W/gr)	308	884	898	611	531	226	101

A systematic decrease in the optimal K_{eff} was observed as the angle ϕ increased from the aligned configuration ($\phi = 0°$). This trend was found for both particle sizes investigated. The largest anisotropy values were required for perfectly oriented particles, whereas progressively smaller values were necessary as the easy axis became increasingly misaligned with the external magnetic field.

This behavior can be understood from the angular dependence of the Zeeman contribution to the Stoner–Wohlfarth energy landscape, $E_Z = -\mu_0 M_s V H cos(\theta - \phi)$.

For particles aligned with the external field ($\phi = 0°$), the magnetic field acts most efficiently in driving magnetization reversal, and the observed loop shape is strongly influenced by the anisotropy barrier. As the orientation angle increases, the projection of the magnetic field along the easy axis decreases, modifying the energy landscape and broadening the switching process. Consequently, a lower anisotropy barrier is required to maintain a comparable dynamic response and preserve loop symmetry.

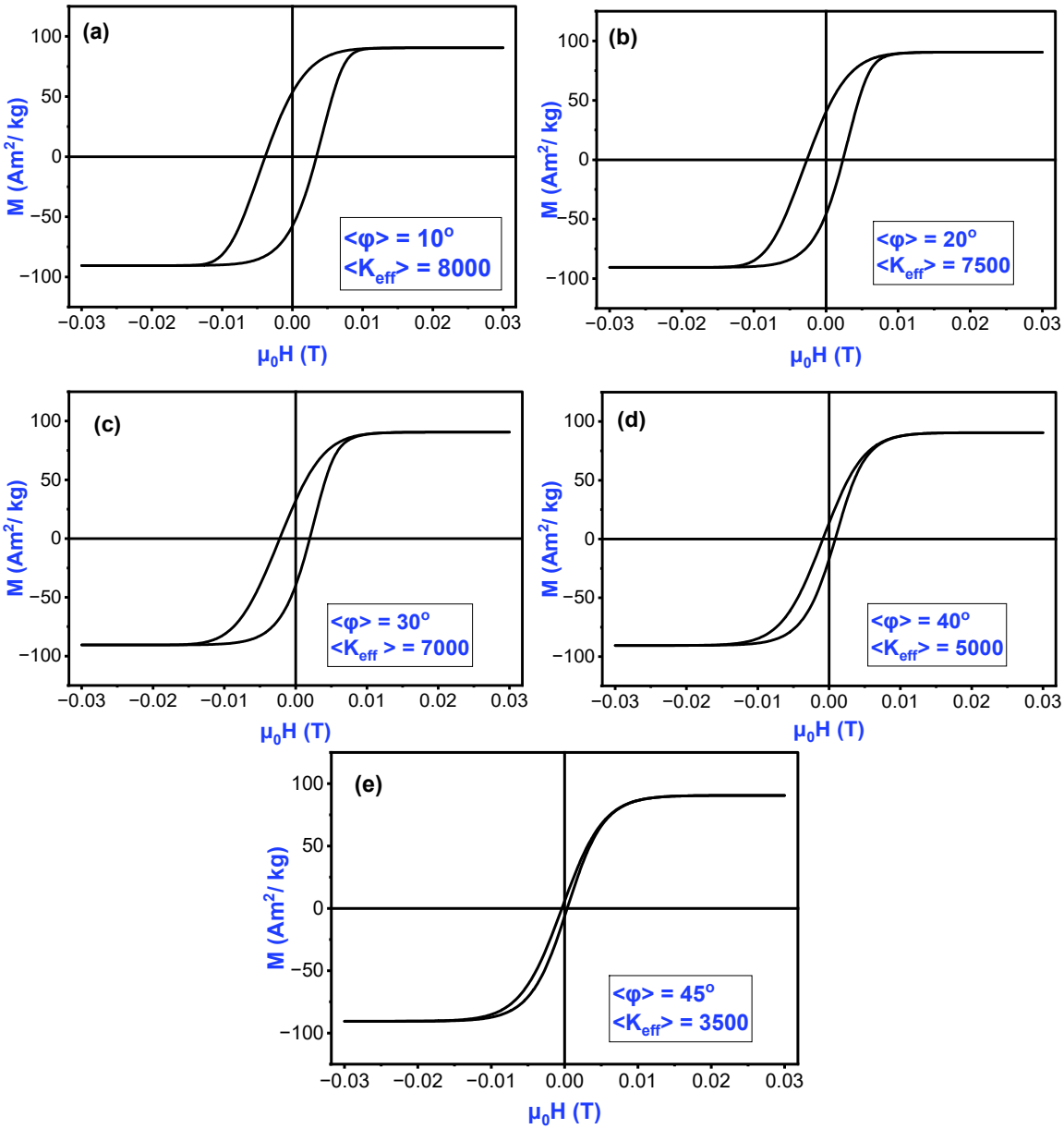


Figure 12. Dynamic hysteresis loops of MNPs with mean diameter 15 nm for various orientations of angle phi (φ) namely for (**a**) 10°, (**b**) 20°, (**c**) 30°, (**d**) 40° and (**e**) 45°. In the inset of each figure we aslo denote the effective anisotropy value in J/m^3 for which the loop was more symmetrica.

As the angle ϕ increases, the magnetic field acquires a transverse component with respect to the anisotropy axis. The magnetization reversal mechanism gradually evolves from purely longitudinal switching toward coherent rotation. This modification of the energy landscape reduces the stability of the two magnetic minima and lowers the effective switching barrier. In other words, the orientational misalignment itself contributes to facilitating magnetization reversal. Therefore, a smaller anisotropy constant is sufficient to generate hysteresis loops with similar symmetry characteristics. The observed reduction in the fitted K_{eff} with increasing ϕ can be interpreted as a manifestation of the reduced effectiveness of the anisotropy energy in constraining the magnetization when the field is no longer applied along the easy axis.

From a physical perspective, this result suggests a partial compensation between anisotropy energy and orientation disorder. Increasing angular misalignment effectively reduces the contribution of the anisotropy term to the observable magnetic response, leading

to a decrease in the apparent or effective anisotropy required to reproduce the experimentally relevant hysteresis behavior. This finding highlights the strong coupling between particle orientation and anisotropy in dynamic magnetic hyperthermia simulations and indicates that anisotropy values extracted from macroscopic magnetic measurements may depend on the degree of orientational disorder present within the nanoparticle ensemble.

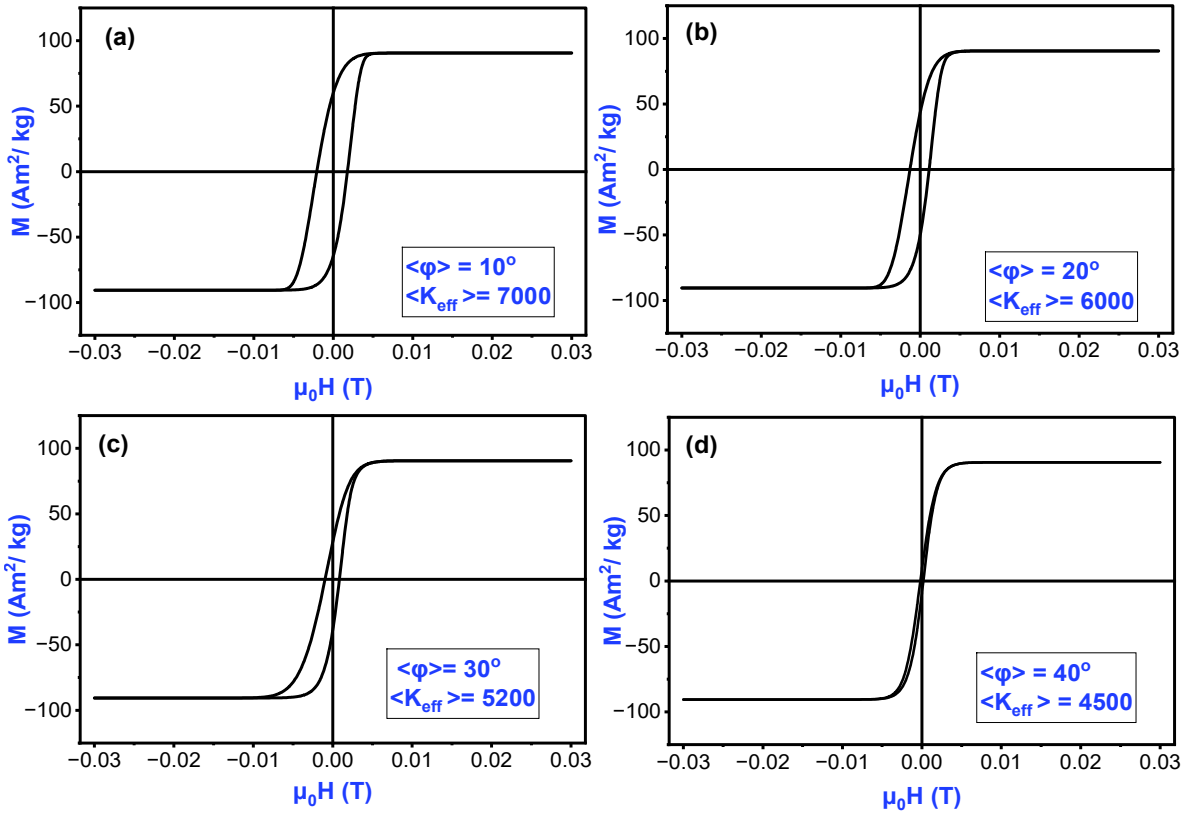


Figure 13. Dynamic hysteresis loops of MNPs with mean diameter 20 nm for various orientations of mean angle φ namely for (**a**) 10°, (**b**) 20°, (**c**) 30°, (**d**) 40°. In the inset of each figure we aslo denote the effective anisotropy value in J/m3 for which the loop was more symmetrical.

The effect was particularly evident for the 15 nm nanoparticles, where thermal activation plays a more significant role because of the smaller magnetic volume and lower energy barriers. For the 20 nm particles, the same trend was observed as observed in Figure 13 and in Table 8, although the larger particle volume partially compensates for the barrier reduction caused by angular misalignment. Nevertheless, both particle sizes exhibited the same qualitative behavior, confirming that the decrease in the effective anisotropy with increasing ϕ is an intrinsic consequence of the angular dependence of the Stoner–Wohlfarth energy landscape rather than a size-specific effect.

These findings further demonstrate the importance of incorporating easy-axis orientation distributions into ensemble calculations. A realistic nanoparticle sample contains particles spanning a wide range of orientations, each characterized by different effective switching barriers and reversal dynamics. Neglecting this orientational variability may therefore lead to significant errors in the predicted hysteresis losses and specific absorption rates. The statistical ensemble approach developed in this work naturally accounts for these effects and provides a more realistic description of magnetic hyperthermia systems.

Table 8. Hysteresis parameters extracted from Figure 13 together with the results that correspond to the loop calculated without distributions and for 20 nm oriented magnetic nanoparticles.

φ (Degrees)	**0**	**0**	**10**	**20**	**30**	**40**
K_{eff} (J/m^3)	**7500 Without Distributions**	**7500**	**7000**	**6000**	**5200**	**4500**
Mr (Am^2/kg)	40.968	69.501	62.272	46.798	39.054	33,569
Ms (Am^2/kg)	90.566	90.566	90.566	90.566	90.566	90.566
Hc (T)	1.20×10^{-3}	3.04×10^{-3}	1.93×10^{-3}	1.20×10^{-3}	1.84×10^{-4}	9.00×10^{-5}
Area (J/kg)	0.4	1.05	0.6	0.3	0.05	0.03
SLP (W/gr)	294	803	479	297	43.3	26

Since we observed that the optimum anisotropy decreased with MNPs average size we decided to also test the 25 and 30 nm to verify the aforementioned trend. In Figures 14 and 15 the dynamic loops for various orientations together with the optimum effective anisotropy value are given for the MNPs diameter values 25 and 30 nm respectevely. Furthermore, the hysteresis characteristics are also depicted in Tables 9 and 10 for those system sizes.

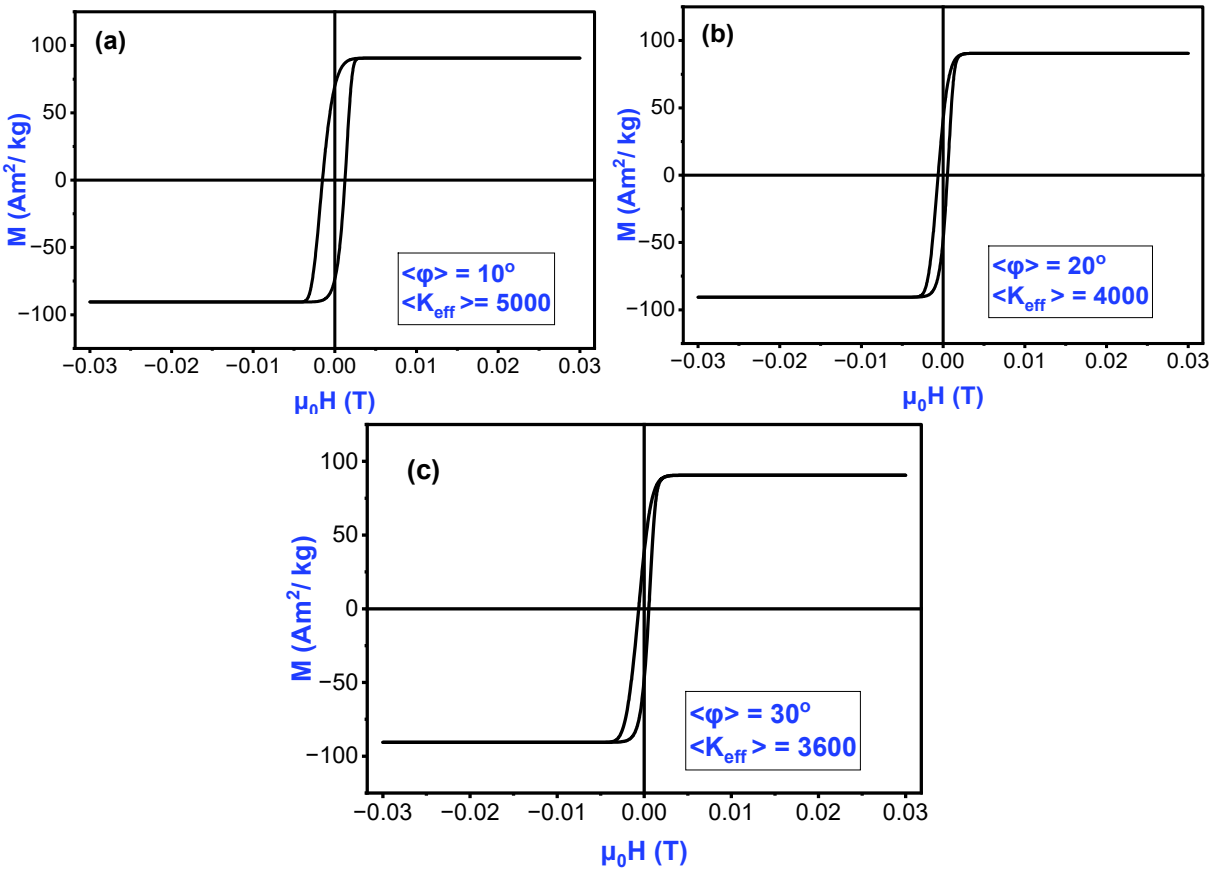


Figure 14. Influence of the orientation angle φ on the dynamic hysteresis loops of MNPs with a mean diameter of 25 nm: (**a**) 10°, (**b**) 20° and (**c**) 30°. The effective anisotropy value in J/m^3 required to maximize loop symmetry is specified in each inset.

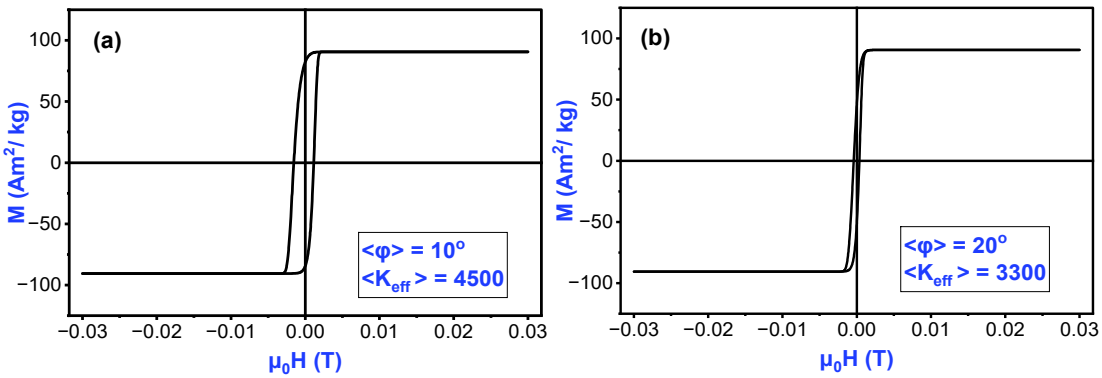


Figure 15. Orientation angle φ dependence of dynamic hysteresis loops for MNPs with 30 nm average size: (**a**) 10°, (**b**) 20°. Insets indicate the effective anisotropy in J/m^3 for maximum loop symmetry.

Table 9. Hysteresis parameters extracted from Figure 14 together with the results that correspond to the loop calculated without distributions and for 25 nm oriented magnetic nanoparticles.

φ (Degrees)	**0**	**0**	**10**	**20**	**30**
Keff (J/m^3)	**6300 Without Distributions**	**6300**	**5000**	**4000**	**3600**
Mr (Am^2/kg)	65.874	84.67	71.685	44.616	43.03
Ms (Am^2/kg)	90.566	90.566	90.566	90.566	90.566
Hc (T)	1.43×10^{-3}	2.40×10^{-3}	1.38×10^{-3}	5.72×10^{-4}	5.72×10^{-4}
Area (J/kg)	0.50	0.8	0.45	0.18	0.18
SLP (W/gr)	369	622	347	140	140

Table 10. Extracted hysteresis parameters from Figure 15 alongside the corresponding values calculated in the absence of distributions for oriented magnetic nanoparticles with a mean diameter of 30 nm.

φ (Degrees)	**0**	**0**	**10**	**20**
Keff (J/m^3)	**5500 Without Distributions**	**5500**	**4500**	**3300**
Mr (Am^2/kg)	84.563	89.811	83.354	48.509
Ms (Am^2/kg)	90.566	90.566	90.566	90.566
Hc (T)	1.91×10^{-3}	2.42×10^{-3}	1.34×10^{-3}	3.78×10^{-4}
Area (J/kg)	0.66	0.86	0.45	0.12
SLP (W/gr)	507	643	345	93.5

A notable observation is that for the fully aligned configuration ($\varphi = \mathbf{0}^\circ$), the hysteresis loop obtained using the distributed model is significantly larger than the corresponding loop predicted by the monodisperse, single-parameter model. In fact, the loop area calculated without distributions was found to be less than half of that obtained when particle size, anisotropy, and orientation distributions were included. To better illustrate this behavior, we present in Figure 16 the dynamic hysteresis loops at $\varphi = 0^\circ$ (oriented particles) with and without distributions for mean diameter values of 15, 20, 25 and 30 nm.

The relatively rapid approach to saturation observed in Figures 12–15, for the lowest mean effective anisotropy values of each MNPs mean size and orientation angle that was examined, originates from the reduction in the anisotropy energy barrier ($\boldsymbol{\Delta E \propto K_{eff} V}$). As the anisotropy decreases, the thermally activated transition rates between the two metastable

states increase, allowing the occupation probabilities to rapidly favor the energetically preferred orientation under the applied field. Consequently, the magnetization reaches its saturation value over a narrower field interval, producing steeper hysteresis-loop segments. Since all investigated parameter combinations satisfy $K_{\mathrm{eff}}V/k_BT > 1$, the nanoparticles remain within the regime where the double-well Néel–Brown description is applicable, and the observed behavior is attributed to reduced magnetic stability rather than to numerical effects.

The results depicted in Figure 16 highlight the limitations of representing a nanoparticle ensemble through a single effective particle. In the monodisperse model, all particles are characterized by identical energy barriers and therefore exhibit similar switching behavior. As a consequence, the magnetic response is restricted to a narrow range of reversal conditions. In contrast, the introduction of statistical distributions generates a broad spectrum of energy barriers and switching fields. While some particles remain magnetically blocked, others possess lower effective barriers and can undergo thermally activated reversal more readily during the field cycle. The collective contribution of these particles broadens the hysteresis loop and increases the energy dissipated per cycle.

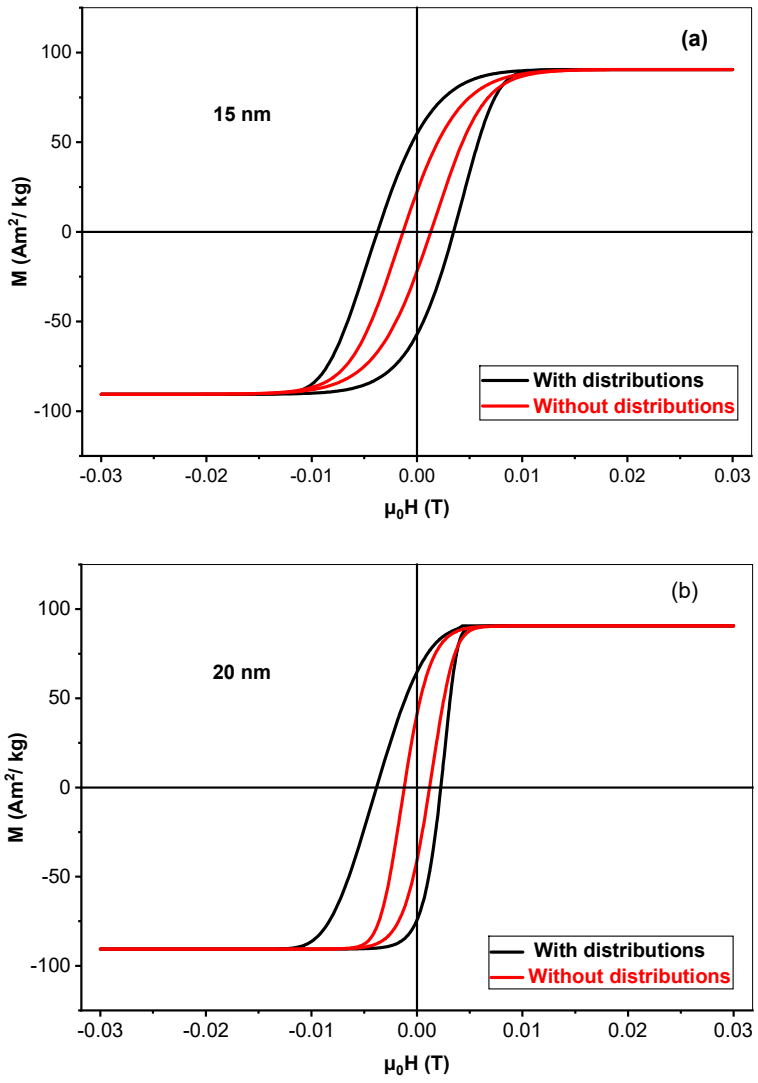


Figure 16. *Cont.*

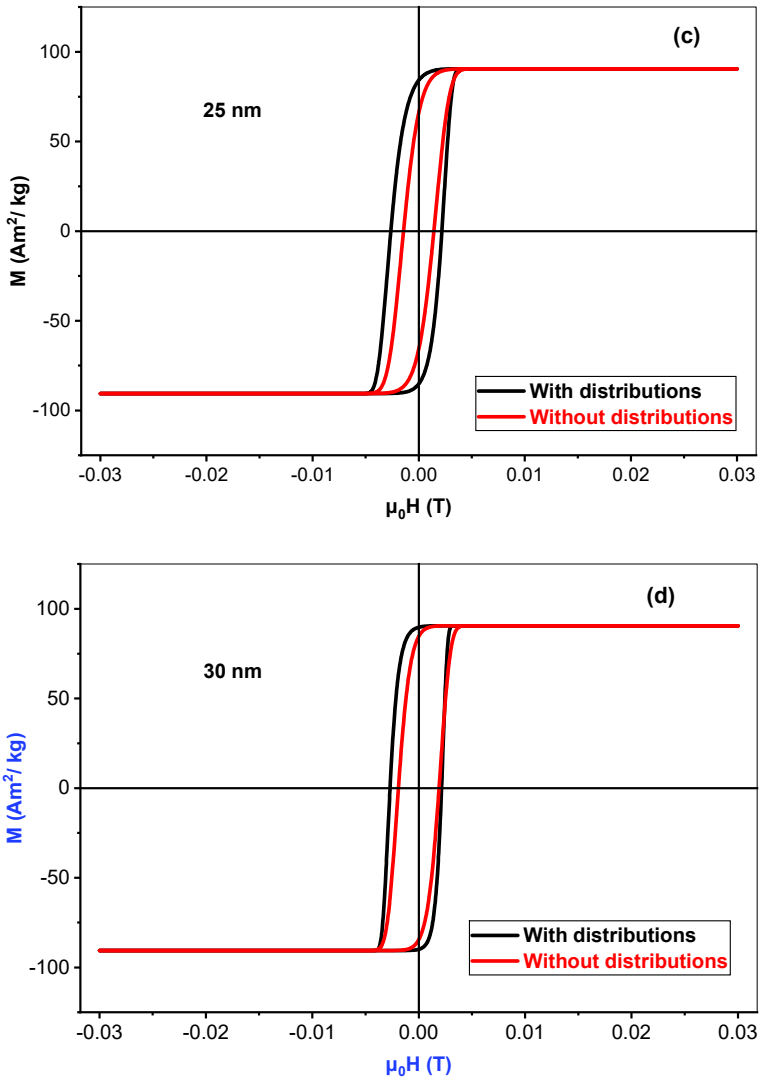


Figure 16. Dynamic hysteresis loops at φ = 0° (oriented particles) with and without distributions for mean diameter values of (**a**) 15, (**b**) 20, (**c**) 25 and (**d**) 30 nm. In the cases with distributions, φ = 0° coincides to the average angle value between the excitation magnetic field and the easy axis.

From a magnetic hyperthermia perspective, this finding demonstrates that ensemble heterogeneity can substantially enhance hysteresis losses compared with predictions based solely on average magnetic properties. The larger loop area obtained after incorporating distributions indicates that a significant fraction of nanoparticles contributes to heating through mechanisms that are not captured by a single-particle approximation. Consequently, models relying exclusively on mean values of particle size and anisotropy may underestimate the actual heating performance of realistic nanoparticle systems.

The effect is particularly pronounced for the aligned configuration ($\boldsymbol{\phi} = \mathbf{0}^\circ$), where the magnetic field couples most efficiently to the nanoparticle easy axis. Under these conditions, the presence of particles with varying anisotropy and volume introduces additional switching pathways, leading to enhanced magnetization reversal and increased hysteresis losses. This observation further supports the inclusion of experimentally realistic distributions when predicting magnetic hyperthermia performance and highlights the importance of ensemble-level modeling for accurate SLP estimation.

An additional trend emerged from the orientation-dependent simulations. For each nanoparticle size, a maximum orientation angle φ_{max} was identified beyond which the dynamic hysteresis loop no longer formed a closed cycle, even when the anisotropy con-

stant was adjusted to the value yielding the highest loop symmetry. The maximum angle decreased systematically with increasing particle diameter, taking values of approximately 45°, 40°, 30°, and 20° for particle diameters of 15, 20, 25, and 30 nm, respectively. The systematic reduction in this critical angle with increasing particle diameter indicates that larger nanoparticles are more sensitive to orientational misalignment. This behavior can be understood in terms of the increasing thermal stability of larger particles. Since the anisotropy energy barrier scales with particle volume ($K_{eff}V \propto D^3$), larger nanoparticles possess higher magnetic stability and exhibit slower thermally activated switching. Simultaneously, increasing the angle between the magnetic field and the anisotropy axis promotes coherent rotational reversal and modifies the topology of the Stoner–Wohlfarth energy landscape. The combined effect of increased magnetic stability and angular misalignment progressively limits the range over which the magnetization dynamics can be accurately represented by a two-state double-well system. Consequently, the maximum angle supporting a stable closed hysteresis loop decreases with increasing particle size. This behavior highlights the growing importance of orientation effects in larger hyperthermia-relevant nanoparticles and further supports the need for statistical ensemble modeling when describing realistic nanoparticle systems.

As the easy axis becomes increasingly misaligned with the applied field, the effective magnetic torque driving reversal is reduced through the angular dependence of the Zeeman term. For small particles, thermal fluctuations remain sufficiently strong to assist magnetization reversal over a relatively broad range of orientations, allowing the hysteresis loop to remain closed even at larger φ. In contrast, larger particles become progressively more constrained by their anisotropy energy landscape and therefore require closer alignment between the easy axis and the applied field to complete a full reversal cycle within the period of the alternating field. Consequently, the maximum orientation angle compatible with a closed dynamic hysteresis loop decreases with increasing particle size. Thus, the growing sensitivity of larger ferromagnetic nanoparticles to orientation disorder suggests that particle alignment may become increasingly important for maximizing magnetic hyperthermia performance as particle size increases. The dependence of the optimized effective magnetic anisotropy constant, for which the loops were symmetrical, (K_{eff}^{opt}) on the easy-axis orientation angle φ is presented in Figure 17 for the four different MNPs diameters (15, 20, 25 and 30 nm) that were tested in this subsection.

In order to straightforwardly evaluate the distributions effect on frequency dependent hysteresis loop, we simulated indicatively a system with (a) lognormal distribution in size with a mean diameter of 15 nm and $\sigma_D = 0.25$ (b) gaussian distribution in effective anisotropy with a mean value of 7000 J/m^3 and $\sigma_K = 0.3$ and (c) also a gaussian distribution for orientation with a mean φ equal to 30° with $\sigma_\varphi = \pi/72$. The results of dynamical hysteresis loops are depicted in Figure 18 together with the hysteresis parameters in Table 11.

Table 11. Characteristic values of hysteresis loops for all the frequency values tested.

Hz (KHz)	50	100	200	300	400	500	765
Mr (Am^2/kg)	3.8404	7.5876	14.7546	20.8995	26.1710	30.6962	40.0007
Ms (Am^2/kg)	90.566	90.566	90.566	90.566	90.566	90,.566	90.566
Hc (T)	0.00018	0.00037	0.00073	0.00107	0.00139	0.00170	0.00243
Area (J/kg)	0.05788	0.11574	0.22996	0.34127	0.44894	0.55368	0.81173
SLP (W/gr)	2894	11.574	45.991	102.382	179.576	276.840	620.977

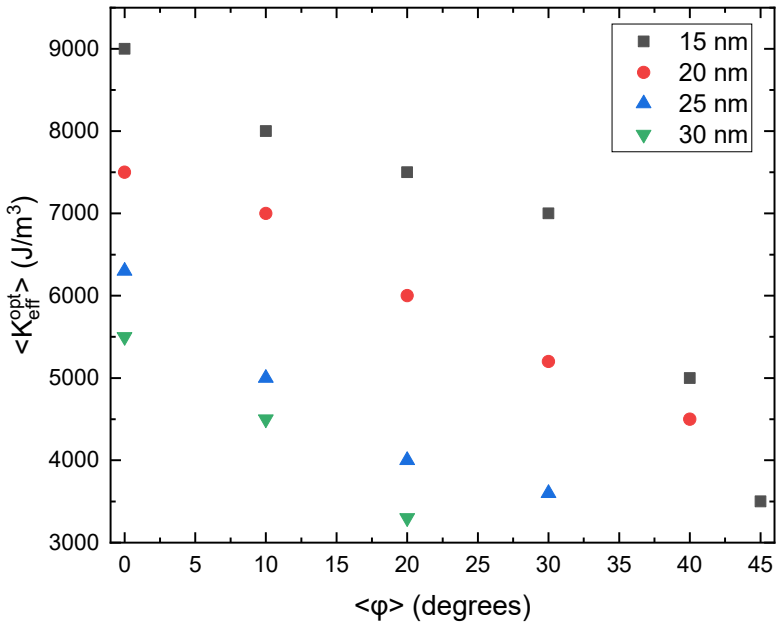


Figure 17. Dependence of the optimum mean effective magnetic anisotropy constant on the mean easy-axis orientation angle for magnetite nanoparticles with diameters of 15, 20, 25, and 30 nm. For each orientation angle, K_{eff} was adjusted to obtain the most symmetric closed dynamic hysteresis loop within the thermally activated Stoner–Wohlfarth framework. A systematic decrease in the optimized anisotropy with increasing angular misalignment is observed for all particle sizes, indicating a compensation between orientation disorder and the anisotropy energy barrier required to maintain physically consistent magnetization reversal dynamics and reflecting the interplay between anisotropy energy and orientation-dependent Zeeman coupling. The maximum angle shown for each particle size corresponds to the largest orientation for which a closed hysteresis loop could be obtained under the applied field conditions of 24 kA/m (0.03 T) and 765 kHz.

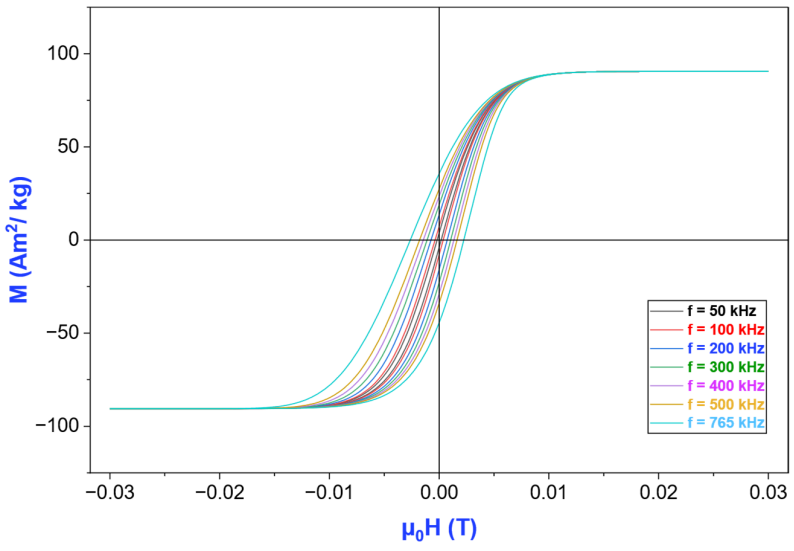


Figure 18. Frequency dependent hysteresis loops obtained from MNPs ensemble where statistical distributions of size, anisotropy and orientation of MNPs were taken into account. The system is characterized by a lognormal distribution in size with a mean diameter of 15 nm and $\sigma_D = 0.25$, a gaussian distribution in effective anisotropy with a mean value of 7000 J/m^3 and $\sigma_K = 0.3$ and also a gaussian distribution for orientation with a mean φ equal to 30° with $\sigma_\varphi = \pi/72$.

Finally, the SLP tendency with frequency for the MNPs system under study is visualized in Figure 19.

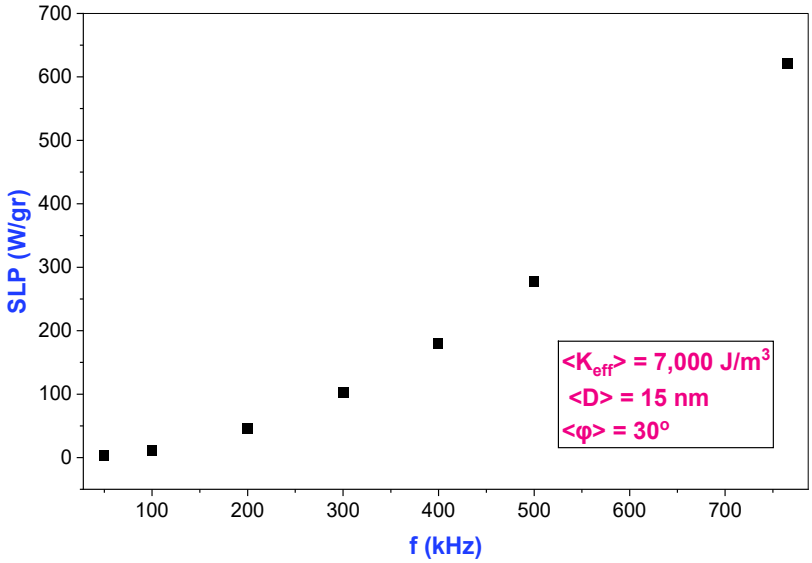


Figure 19. SLP spectrum for the specified MNPs system with statistical distributions of size, effective anisotropy and orientation angle.

Note here that the observation of saturated hysteresis loops for the cases where the applied field amplitude was lower than the anisotropy field H_K is a consequence of the dynamic and thermally activated nature of the present model. In the classical zero-temperature Stoner–Wohlfarth model, complete magnetization reversal is expected only when the applied field approaches the angular-dependent switching field, which may be comparable to the anisotropy field. However, the framework employed here incorporates Néel thermal activation through Arrhenius-type transition probabilities. Consequently, magnetization reversal is not determined solely by the instantaneous field magnitude but also by the time-dependent probability of overcoming the anisotropy energy barrier.

At the frequencies and temperatures considered, thermally activated switching progressively depopulates metastable states during each field cycle, allowing a large fraction of particles to align with the external field even when the applied field remains below the nominal anisotropy field. Furthermore, the inclusion of particle size, anisotropy, and orientation distributions broadens the ensemble switching field distribution. A significant fraction of nanoparticles possess effective energy barriers lower than the ensemble average and therefore switch at fields substantially below H_K. As a result, the ensemble magnetization approaches saturation over an extended field range, producing the long saturation regions observed in the simulated loops.

It should also be noted that the anisotropy field $H_K = 2K_{eff}/\mu_0 Ms$ represents a characteristic quantity derived for an ideal single particle with a specific orientation. In a distributed ensemble subjected to thermal activation, the onset and completion of magnetization reversal occur over a broad field interval rather than at a single critical field. Therefore, the observation of near-saturated dynamic hysteresis loops for field amplitudes below the nominal anisotropy field is physically consistent with the thermally activated Stoner–Wohlfarth framework employed in this study.

4. Discussion

The present work developed a statistical ensemble framework for the estimation of dynamic hysteresis loops in single-domain ferromagnetic nanoparticles subjected to alternating magnetic fields. The model combines the Stoner–Wohlfarth description of the magnetic energy landscape with the Néel–Brown theory of thermally activated magnetization reversal through a double-well rate-equation formalism. Two implementations were

investigated: an idealized model of perfectly oriented nanoparticles with identical magnetic properties and a more realistic statistical ensemble model incorporating distributions of particle size, magnetic anisotropy, and easy-axis orientation.

The results obtained for the oriented nanoparticle system demonstrate the strong dependence of dynamic hysteresis on the intrinsic magnetic properties of the nanoparticles and on the characteristics of the applied magnetic field. Increasing the anisotropy constant resulted in a systematic increase in coercivity, remanence, hysteresis area, and specific loss power. This behavior is consistent with the Stoner–Wohlfarth theory, according to which the anisotropy energy determines the stability of the magnetic states and controls the height of the energy barriers separating the two minima. Since the Néel relaxation time depends exponentially on the energy barrier, even moderate variations in anisotropy produce significant changes in the probability of thermally activated transitions and consequently in the shape of the hysteresis loop. Similar trends have been reported in both experimental and theoretical studies of magnetic hyperthermia, where an optimum anisotropy range is often observed for maximizing energy dissipation under clinically acceptable magnetic field amplitudes.

The particle-size dependence observed in the present study can also be directly related to the energy-barrier formulation. Since the anisotropy energy scales with particle volume, the barrier height is proportional to ($K_{eff}V$), and therefore approximately proportional to (KD^3). As a result, small variations in diameter lead to substantial modifications of thermal stability and magnetic relaxation. The calculated increase in hysteresis area and SLP with particle size agrees with previous investigations demonstrating the critical role of nanoparticle volume in determining hyperthermia performance. The strong size dependence observed in the present work further highlights the importance of accurately characterizing particle-size distributions when interpreting experimental measurements.

The influence of excitation frequency followed the expected dynamic behavior of thermally activated magnetic systems. Increasing the frequency produced larger hysteresis loops and higher energy losses because the characteristic timescale of the applied magnetic field becomes increasingly comparable to the characteristic relaxation time of the nanoparticles. Under such conditions, the magnetization is unable to fully equilibrate during each field cycle, leading to increased phase lag and larger hysteresis losses. This behavior is consistent with the predictions of dynamic hysteresis theory and has been widely observed in experimental hyperthermia studies.

Temperature was found to exert a strong influence on magnetic losses. Increasing temperature reduced coercivity, remanence, hysteresis area, and SLP, indicating enhanced thermal activation between the two metastable states. This result is a direct consequence of the Arrhenius dependence of the transition rates on the ratio $\Delta E/k_BT$. As thermal energy increases, transitions between the wells become more frequent, reducing magnetic irreversibility and facilitating equilibration of the magnetization. The observed temperature dependence therefore confirms the physical consistency of the double-well rate-equation framework.

A particularly important outcome of the present work is the systematic investigation of easy-axis orientation effects. For all the average sizes tested, 15–30 nm nanoparticles, the effective anisotropy required to produce symmetric hysteresis loops decreased as the angle between the magnetic field and the anisotropy axis increased. This trend can be understood from the angular dependence of the Stoner–Wohlfarth switching field. In the aligned configuration $\varphi = 0^\circ$, the anisotropy energy acts directly against magnetization reversal and the energy barriers attain their maximum values. As the easy axis rotates away from the field direction, the switching field decreases and the magnetization reversal process increasingly involves coherent rotation rather than purely longitudinal switching. Consequently, the

energy landscape becomes progressively less stable and smaller anisotropy values are sufficient to generate hysteresis loops with comparable symmetry characteristics.

The decrease in the effective anisotropy with increasing orientation angle is therefore not merely a fitting artifact but rather a manifestation of the underlying angular dependence of the magnetic energy landscape. The observation that the same qualitative trend was obtained for both nanoparticle sizes indicates that this behavior is an intrinsic consequence of the Stoner–Wohlfarth model. These findings further emphasize the importance of considering orientation effects when interpreting magnetic hyperthermia experiments, particularly for liquid suspensions and powder samples where the nanoparticles are randomly distributed.

The incorporation of statistical distributions revealed substantial differences compared with the idealized oriented-particle model. In particular, the inclusion of particle-size and anisotropy distributions generally increased the hysteresis area and the predicted heating efficiency. This behavior originates from the highly nonlinear dependence of the transition rates on the energy barrier. Since the relaxation time depends exponentially on ($K_{eff}V$), nanoparticles located in the upper tails of the size and anisotropy distributions contribute disproportionately to the overall magnetic losses. Consequently, the response of a realistic nanoparticle ensemble cannot be accurately represented by a hypothetical particle possessing average properties.

This observation has important implications for magnetic hyperthermia modeling. In many analytical approaches, average values of particle size and anisotropy are substituted directly into the governing equations. While such approximations may provide qualitative trends, they neglect the nonlinear nature of the underlying physics. The present results demonstrate that ensemble averaging must be performed after the individual nanoparticle response has been calculated, rather than replacing the ensemble with a single average particle. This distinction becomes particularly important when broad size or anisotropy distributions are present.

One of the major strengths of the proposed framework is its ability to model realistic nanoparticle populations while maintaining a computational cost that remains several orders of magnitude lower than that of full micromagnetic simulations. Although micromagnetic methods based on the Landau–Lifshitz–Gilbert equation provide detailed information regarding magnetization dynamics, they are generally limited to relatively small systems because of their computational requirements. In contrast, a typical hyperthermia sample may contain more than 10^{13} nanoparticles per milligram. Directly simulating such systems at the particle level is currently impractical. The statistical ensemble methodology developed here addresses this challenge by replacing the explicit simulation of every nanoparticle with a probability-based description of the ensemble.

An additional advantage of the present approach is the preservation of a direct connection between microscopic and macroscopic behavior. The energy barriers, transition rates, occupation probabilities, and hysteresis losses can all be traced back to physically meaningful quantities derived from the Stoner–Wohlfarth energy landscape. This level of physical transparency is often more difficult to achieve in large-scale numerical simulations, where the underlying mechanisms may be obscured by the complexity of the calculations.

Despite these advantages, several limitations should be acknowledged. The current model assumes non-interacting nanoparticles and therefore neglects dipolar interactions that may become significant at high particle concentrations. Furthermore, the double-well approximation assumes coherent magnetization reversal and does not account for nonuniform magnetization configurations that may arise in larger particles. The anisotropy was also assumed to be effectively uniaxial, whereas real nanoparticles may exhibit more

complex anisotropy contributions arising from crystal structure, shape effects, surface disorder, and interfacial phenomena.

For some parameter combinations, particularly for low effective anisotropy values, the maximum applied field may exceed the nominal anisotropy field. In these cases, the double-well formulation should be interpreted as an effective two-state description of magnetization reversal rather than a strict representation of a permanently bistable energy landscape. The model should therefore be regarded as a coarse-grained stochastic representation of the magnetic dynamics rather than a strict instantaneous double-well description. Despite this limitation, the model successfully reproduces the expected dependence of hysteresis losses on anisotropy, particle size, frequency, temperature, and orientation, supporting its usefulness as a computationally efficient framework for describing dynamic hysteresis in nanoparticle ensembles. Moreover, the applicability of the double-well rate-equation framework was assessed through the dimensionless parameter $K_{eff}V/k_BT$. For all parameter combinations considered in the present study, this ratio exceeded unity, indicating that the anisotropy energy dominates over thermal fluctuations and that the nanoparticles exhibit two thermally stable magnetic states. Consequently, the magnetization dynamics can be described within the Néel–Brown two-state formalism and the associated rate-equation approach which is a simplifying approximation to the Fokker–Planck equation for the double-well problem [53,54]. For magnetic nanoparticles, rate equations were shown [28] to naturally emerge from the Fokker–Planck equation when the ratio $K_{eff}V/k_BT$ is larger than unity; therefore, the validity of the approach at a given temperature depends on both magnetic anisotropy and nanoparticle size.

The present double-well rate-equation framework occupies an intermediate position between fully microscopic stochastic approaches and simplified linear response descriptions. In contrast to stochastic Landau–Lifshitz–Gilbert simulations, which resolve the continuous precessional dynamics of individual magnetic moments, and Fokker–Planck approaches, which solve the full probability density evolution in orientation space, the present model reduces the problem to transitions between two metastable states defined by the Stoner–Wohlfarth energy landscape. This coarse-graining significantly reduces computational cost while preserving the essential physics of thermally activated magnetization reversal. Compared to linear response theory, which is valid only in the small-field regime, the present approach remains applicable in the nonlinear regime where hysteresis and irreversible losses dominate. Therefore, the model provides a computationally efficient alternative for exploring dynamic hysteresis in large nanoparticle ensembles, where fully stochastic approaches become computationally prohibitive.

The relatively rapid approach to magnetic saturation observed in the simulated hysteresis loops arises from the intrinsic characteristics of the thermally activated Stoner–Wohlfarth (SW) model under strong external fields and from the nature of the nanoparticle ensemble considered. In the present framework, each nanoparticle is treated as a single-domain macrospin with uniaxial anisotropy, and the magnetization dynamics are governed by the competition between anisotropy energy and Zeeman energy. Under increasing applied magnetic field, the Zeeman term rapidly dominates the energy landscape when $\mu_0 M_s H \gtrsim K_{eff}$, leading to the progressive destabilization of metastable states. For the magnetite parameters considered (15–30 nm particles and 3 $kJ/m^3 < K_{eff} < 20$ kJ/m^3 this crossover occurs at relatively moderate field amplitudes, resulting in fast alignment of magnetic moments with the external field direction. Additionally, the ensemble averaging over particle size, anisotropy, and orientation distributions contributes to a two-stage saturation behavior observed in the loops. The first, rapid saturation at low fields originates from the subset of particles with favorable orientations ($\phi \approx 0$) and lower effective energy barriers, which switch readily under small applied fields. The second, slower approach to full saturation is

associated with particles having less favorable orientations and higher anisotropy barriers, which require larger fields to fully align. This produces the characteristic "fast + gradual" saturation behavior observed in the simulated loops. Thermal activation further smooths the transition between metastable states, allowing partial switching at fields below the deterministic Stoner–Wohlfarth switching field. This reduces coercive sharpness and contributes to an earlier apparent saturation in the ensemble magnetization curve. Finally, it should be emphasized that the observed behavior is consistent with the expected response of non-interacting single-domain nanoparticles under strong AC excitation and does not indicate premature numerical saturation. Instead, it reflects the combined effects of anisotropy-field competition, orientation disorder, and thermally activated switching dynamics inherent to the model.

It should be noted that all hysteresis loops reach the same saturation magnetization value, as the simulations assume a fixed intrinsic saturation magnetization M_s for magnetite nanoparticles. The present model focuses on the thermally activated reversal dynamics of single-domain particles, and therefore variations in particle size, anisotropy, temperature, and field frequency affect the loop shape (coercivity, remanence, and area) rather than the saturation magnetization itself. Consequently, differences between the hysteresis curves reflect changes in magnetization reversal kinetics rather than changes in the intrinsic magnetic moment of the nanoparticles. The predicted behavior is consistent with experimental observations [27,55,56] in single-domain magnetite nanoparticle systems, where the saturation magnetization remains approximately constant for a given material, while hysteresis losses and coercivity vary significantly with particle size distribution, anisotropy, and temperature.

The relatively high specific loss power (SLP) values obtained in certain parameter regimes should be interpreted as theoretical upper limits within the present single-particle framework. In experimental systems, the effective SLP is typically reduced by factors not included in the present model, such as dipolar interactions, aggregation effects, hydrodynamic constraints, and size/anisotropy dispersions beyond the assumed distributions. Nevertheless, values in the range of several thousand W/g have been reported experimentally in optimized nanoparticle systems [57–61], indicating that the present predictions correspond to physically accessible upper-bound regimes under favorable conditions.

Future work could extend the present framework in several directions. The inclusion of dipolar interactions through mean-field or pair-interaction approaches would allow investigation of concentrated nanoparticle systems. Additional extensions could incorporate distributions of saturation magnetization, exchange-coupled multicore nanoparticles, temperature-dependent anisotropy, and field-dependent energy barriers obtained from exact numerical solutions of the Stoner–Wohlfarth energy landscape. The Stoner–Wohlfarth (SW) approach is of central importance in the present framework as it provides the fundamental theoretical description of magnetization reversal in single-domain, non-interacting ferromagnetic nanoparticles with uniaxial anisotropy. Within this model, magnetic switching is governed by the competition between anisotropy energy and Zeeman energy, leading to well-defined metastable states and energy barriers that can be treated analytically. This makes the SW model particularly suitable for magnetic hyperthermia applications in the single-domain size regime (typically 10–30 nm for magnetite), where coherent rotation dominates magnetization dynamics. In the present work, the SW formalism enables a physically transparent description of hysteresis formation under alternating magnetic fields, while its extension with thermal Néel activation allows the inclusion of finite-temperature effects relevant to biomedical conditions. Importantly, the SW framework provides a direct link between microscopic material parameters (K, Ms, particle size, and orientation) and macroscopic observables such as coercivity, loop area, and specific loss power

(SLP), making it highly valuable for predictive modeling and nanoparticle optimization in magnetic hyperthermia.

Furthermore, direct comparisons with experimental hyperthermia measurements would provide an important validation of the model and could facilitate the extraction of effective magnetic parameters from measured hysteresis loops.

Overall, the results demonstrate that the statistical ensemble double-well rate-equation approach provides a physically consistent and computationally efficient framework for describing dynamic hysteresis in single-domain ferromagnetic nanoparticles. By combining thermally activated switching, orientation effects, and realistic distributions of nanoparticle properties within a unified formalism, the model offers a valuable tool for investigating magnetic hyperthermia systems and for understanding the relationship between nanoparticle characteristics and magnetic energy dissipation.

5. Conclusions

This work presents a statistical ensemble double-well rate-equation framework for modeling dynamic hysteresis in single-domain ferromagnetic nanoparticles under alternating magnetic fields. The model bridges Stoner–Wohlfarth energy landscapes with Néel–Brown thermally activated dynamics while enabling efficient computation of large nanoparticle ensembles with distributed size, anisotropy, and orientation. The results demonstrate that magnetic anisotropy, particle size, excitation frequency, temperature, and easy-axis orientation critically determine hysteresis losses and specific loss power. In particular, the inclusion of realistic distributions leads to significant deviations from single-parameter predictions due to the nonlinear dependence of transition rates on energy barriers. The model further shows that orientation effects impose a size-dependent trend on the stability of closed hysteresis loops, highlighting the importance of statistical averaging in realistic systems. While the present framework neglects interparticle interactions and Brownian rotation, it provides a computationally efficient and physically transparent tool for predicting magnetic hyperthermia performance in dilute nanoparticle systems and for guiding experimental design of optimized magnetic nanoheaters.

Author Contributions: Conceptualization, N.M., I.K., N.V. and M.M.; methodology, N.M., I.K., N.V. and M.M.; software, N.M., I.K., N.V. and M.M.; validation, N.M., I.K., N.V. and M.M.; formal analysis, N.M., I.K., N.V. and M.M.; investigation, N.M., I.K., N.V. and M.M.; resources, N.M., I.K., N.V. and M.M.; data curation, N.M., I.K., N.V. and M.M.; writing—original draft preparation, N.M., I.K., N.V. and M.M.; writing—review and editing, N.M., I.K., N.V. and M.M.; visualization, N.M., I.K., N.V. and M.M.; project administration, N.M., I.K., N.V. and M.M. All authors have read and agreed to the published version of the manuscript.

Funding: This research received no external funding.

Institutional Review Board Statement: Not applicable.

Informed Consent Statement: Not applicable.

Data Availability Statement: Data supporting reported results can be found in https://github.com/IoannaKranioti/Single-Domain-Magnetic-Nanoparticle-Simulation, accessed on 17 June 2026.

Conflicts of Interest: The authors declare no conflicts of interest.

References

1. Mauter, M.S.; Zucker, I.; Perreault, F.; Werber, J.R.; Kim, J.H.; Elimelech, M. The Role of Nanotechnology in Tackling Global Water Challenges. *Nat. Sustain.* **2018**, *1*, 166–175. [CrossRef]
2. Vamvakidis, K.; Katsikini, M.; Vourlias, G.; Angelakeris, M.; Paloura, E.C.; Dendrinou-Samara, C. Composition and Hydrophilicity Control of Mn-Doped Ferrite ($Mn_xFe_{3-x}O_4$) Nanoparticles Induced by Polyol Differentiation. *Dalt. Trans.* **2015**, *44*, 5396–5406. [CrossRef] [PubMed]
3. Tay, Z.W.; Chandrasekharan, P.; Chiu-Lam, A.; Hensley, D.W.; Dhavalikar, R.; Zhou, X.Y.; Yu, E.Y.; Goodwill, P.W.; Zheng, B.; Rinaldi, C.; et al. Magnetic Particle Imaging-Guided Heating in Vivo Using Gradient Fields for Arbitrary Localization of Magnetic Hyperthermia Therapy. *ACS Nano* **2018**, *12*, 3699–3713. [CrossRef] [PubMed]
4. Bendre, A.; Somasekhara, D.; Nadumane, V.K.; Sriram, G.; Bilimagga, R.S.; Kurkuri, M.D. Design and Application of Microfluidic Capture Device for Physical–Magnetic Isolation of MCF-7 Circulating Tumor Cells. *Biosensors* **2024**, *14*, 308. [CrossRef] [PubMed]
5. Materón, E.M.; Miyazaki, C.M.; Carr, O.; Joshi, N.; Picciani, P.H.S.; Dalmaschio, C.J.; Davis, F.; Shimizu, F.M. Magnetic Nanoparticles in Biomedical Applications: A Review. *Appl. Surf. Sci. Adv.* **2021**, *6*, 100163. [CrossRef]
6. Rubia-Rodríguez, I.; Santana-Otero, A.; Spassov, S.; Tombácz, E.; Johansson, C.; De La Presa, P.; Teran, F.J.; Morales, M.D.P.; Veintemillas-Verdaguer, S.; Thanh, N.T.K.; et al. Whither Magnetic Hyperthermia? A Tentative Roadmap. *Materials* **2021**, *14*, 706. [CrossRef] [PubMed]
7. Charra, F.; Gota-Goldmann, S.; Warlimont, H. Nanostructured Materials. In *Springer Handbooks*; Springer: Cham, Switzerland, 2018.
8. Nabil, M.; Decuzzi, P.; Zunino, P. Modelling Mass and Heat Transfer in Nano-Based Cancer Hyperthermia. *R. Soc. Open Sci.* **2015**, *2*, 150447. [CrossRef] [PubMed]
9. Brzuszek, K.; Ross, C.A.; Janutka, A. High-Frequency Magnetic Response of Superparamagnetic Composites of Spherical Fe and Fe_3O_4 Nanoparticles. *J. Magn. Magn. Mater.* **2024**, *599*, 172070. [CrossRef]
10. Simeonidis, K.; Martinez-Boubeta, C.; Serantes, D.; Ruta, S.; Chubykalo-Fesenko, O.; Chantrell, R.; Oró-Solé, J.; Balcells, L.; Kamzin, A.S.; Nazipov, R.A.; et al. Controlling Magnetization Reversal and Hyperthermia Efficiency in Core-Shell Iron-Iron Oxide Magnetic Nanoparticles by Tuning the Interphase Coupling. *ACS Appl. Nano Mater.* **2020**, *3*, 4465–4476. [CrossRef] [PubMed]
11. Jalal, E.M.; Saadi, H.; Hasnaoui, A.; Hachem, O.; Lafhal, A.; Madani, M.; El Bouziani, M. Single-Ion Anisotropy Effect on the Critical and Hysteresis Behaviors of a Mixed-Spin (1, 3/2) Square Ising Nanowire. *Phys. Status Solidi Basic Res.* **2023**, *260*, 2300180. [CrossRef]
12. Ekramian, E.; Etemad, S.G.; Haghshenasfard, M. Numerical Investigations of Heat Transfer Performance of Nanofluids in a Flat Plate Solar Collector. *Int. J. Theor. Appl. Nanotechnol.* **2014**, *2*, 30–39. [CrossRef]
13. Sundara Mahalingam, S.; Manikandan, B.V.; Arockiaraj, S. Review-Micromagnetic Simulation Using OOMMF and Experimental Investigations on Nano Composite Magnets. *J. Phys. Conf. Ser.* **2019**, *1172*, 012070.
14. Ferrero, R.; Vicentini, M.; Manzin, A. Influence of Size, Volume Concentration and Aggregation State on Magnetic Nanoparticle Hyperthermia Properties versus Excitation Conditions. *Nanoscale Adv.* **2024**, *6*, 1739–1749. [CrossRef] [PubMed]
15. Haase, C.; Nowak, U. Role of Dipole-Dipole Interactions for Hyperthermia Heating of Magnetic Nanoparticle Ensembles. *Phys. Rev. B-Condens. Matter Mater. Phys.* **2012**, *85*, 045435. [CrossRef]
16. Maniotis, N. Studying the Rate-Dependent Specific Absorption Rate in Magnetic Hyperthermia through Multiscale Simulations. *AIP Adv.* **2023**, *13*, 065122. [CrossRef]
17. Leliaert, J.; Mulkers, J. Tomorrow's Micromagnetic Simulations. *J. Appl. Phys.* **2019**, *125*, 180901. [CrossRef]
18. Tseng, P.; Judy, J.W.; Di Carlo, D. Magnetic Nanoparticle-Mediated Massively Parallel Mechanical Modulation of Single-Cell Behavior. *Nat. Methods* **2012**, *9*, 1113–1119. [CrossRef] [PubMed]
19. Bjørk, R.; Poulsen, E.B.; Nielsen, K.K.; Insinga, A.R. MagTense: A Micromagnetic Framework Using the Analytical Demagnetization Tensor. *J. Magn. Magn. Mater.* **2021**, *535*, 168057. [CrossRef]
20. Zhigilei, L.V.; Volkov, A.N.; Dongare, A.M. Computational Study of Nanomaterials: From Large-Scale Atomistic Simulations to Mesoscopic Modeling. In *Encyclopedia of Nanotechnology*; Springer: Dordrecht, The Netherlands, 2016.
21. Gavilán, H.; Simeonidis, K.; Myrovali, E.; Mazarío, E.; Chubykalo-Fesenko, O.; Chantrell, R.; Balcells, L.; Angelakeris, M.; Morales, M.P.; Serantes, D. How Size, Shape and Assembly of Magnetic Nanoparticles Give Rise to Different Hyperthermia Scenarios. *Nanoscale* **2021**, *13*, 15631–15646. [CrossRef] [PubMed]
22. Manzin, A.; Ferrero, R.; Vicentini, M. From Micromagnetic to In Silico Modeling of Magnetic Nanodisks for Hyperthermia Applications. *Adv. Theory Simul.* **2021**, *4*, 2100013. [CrossRef]
23. Vallejo-Fernandez, G.; Ogrady, K. Effect of the Distribution of Anisotropy Constants on Hysteresis Losses for Magnetic Hyperthermia Applications. *Appl. Phys. Lett.* **2013**, *103*, 142417. [CrossRef]
24. Saville, S.L.; Qi, B.; Baker, J.; Stone, R.; Camley, R.E.; Livesey, K.L.; Ye, L.; Crawford, T.M.; Thompson Mefford, O. The Formation of Linear Aggregates in Magnetic Hyperthermia: Implications on Specific Absorption Rate and Magnetic Anisotropy. *J. Colloid Interface Sci.* **2014**, *424*, 141–151. [CrossRef] [PubMed]

25. Gazeau, F.; Bacri, J.C.; Gendron, F.; Perzynski, R.; Raikher, Y.L.; Stepanov, V.I.; Dubois, E. Magnetic Resonance of Ferrite Nanoparticles: Evidence of Surface Effects. *J. Magn. Magn. Mater.* **1998**, *186*, 175–187. [CrossRef]
26. Bian, B.; Chen, G.; Zheng, Q.; Du, J.; Lu, H.; Liu, J.P.; Hu, Y.; Zhang, Z. Self-Assembly of CoPt Magnetic Nanoparticle Arrays and Its Underlying Forces. *Small* **2018**, *14*, 1801184. [CrossRef] [PubMed]
27. Carrey, J.; Mehdaoui, B.; Respaud, M. Simple models for dynamic hysteresis loop calculations of magnetic single-domain nanoparticles: Application to magnetic hyperthermia optimization. *J. Appl. Phys.* **2011**, *109*, 083921. [CrossRef]
28. Allia, P.; Barrera, G.; Tiberto, P. Nonharmonic Driving Fields for Enhancement of Nanoparticle Heating Efficiency in Magnetic Hyperthermia. *Phys. Rev. Appl.* **2019**, *12*, 034041. [CrossRef]
29. Allia, P.; Barrera, G.; Tiberto, P. Linearized Rate-Equation Approach for Double-Well Systems: Cooling- and Temperature-Dependent Low-Field Magnetization of Magnetic Nanoparticles. *Phys. Rev. B* **2018**, *98*, 134423. [CrossRef]
30. Barrera, G.; Allia, P.; Tiberto, P. Multifunctional Effects in Magnetic Nanoparticles for Precision Medicine: Combining Magnetic Particle Thermometry and Hyperthermia. *Nanoscale Adv.* **2023**, *5*, 4080–4094. [CrossRef] [PubMed]
31. Maniotis, N.; Maragakis, M.; Vordos, N. A Comprehensive Analysis of Nanomagnetism Models for the Evaluation of Particle Energy in Magnetic Hyperthermia. *Nanoscale Adv.* **2025**, *7*, 4252–4269. [CrossRef] [PubMed]
32. Maniotis, N.; Simeonidis, K. Analytical Approaches of Magnetic Hybrid Nanoparticles Using Numerical Modelling and Simulation Tools. In *Handbook of Magnetic Hybrid Nanoalloys and Their Nanocomposites*; Springer: Cham, Switzerland, 2022; ISBN 9783030909482.
33. Engelmann, U.M.; Shasha, C.; Teeman, E.; Slabu, I.; Krishnan, K.M. Predicting Size-Dependent Heating Efficiency of Magnetic Nanoparticles from Experiment and Stochastic Néel-Brown Langevin Simulation. *J. Magn. Magn. Mater.* **2018**, *471*, 450–456. [CrossRef]
34. Ruta, S.; Chantrell, R.; Hovorka, O. Unified Model of Hyperthermia via Hysteresis Heating in Systems of Interacting Magnetic Nanoparticles. *Sci. Rep.* **2015**, *5*, 9090. [CrossRef] [PubMed]
35. Cobianchi, M.; Guerrini, A.; Avolio, M.; Innocenti, C.; Corti, M.; Arosio, P.; Orsini, F.; Sangregorio, C.; Lascialfari, A. Experimental Determination of the Frequency and Field Dependence of Specific Loss Power in Magnetic Fluid Hyperthermia. *J. Magn. Magn. Mater.* **2017**, *444*, 154–160. [CrossRef]
36. Hadadian, Y.; Ramos, A.P.; Pavan, T.Z. Role of Zinc Substitution in Magnetic Hyperthermia Properties of Magnetite Nanoparticles: Interplay between Intrinsic Properties and Dipolar Interactions. *Sci. Rep.* **2019**, *9*, 18048. [CrossRef] [PubMed]
37. Lacroix, L.M.; Malaki, R.B.; Carrey, J.; Lachaize, S.; Respaud, M.; Goya, G.F.; Chaudret, B. Magnetic Hyperthermia in Single-Domain Monodisperse FeCo Nanoparticles: Evidences for Stoner-Wohlfarth Behavior and Large Losses. *J. Appl. Phys.* **2009**, *105*, 023911. [CrossRef]
38. Rodrigo, I.; Castellanos-Rubio, I.; Garaio, E.; Arriortua, O.K.; Insausti, M.; Orue, I.; García, J.Á.; Plazaola, F. Exploring the Potential of the Dynamic Hysteresis Loops via High Field, High Frequency and Temperature Adjustable AC Magnetometer for Magnetic Hyperthermia Characterization. *Int. J. Hyperth.* **2020**, *37*, 976–991. [CrossRef] [PubMed]
39. Wolfram. Wolfram Mathematica: Modern Technical Computing. Available online: https://www.wolfram.com/mathematica/ (accessed on 1 June 2026).
40. Stoner, E.C.; Wohlfarth, E.P. A Mechanism of Magnetic Hysteresis in Heterogeneous Alloys. *Philos. Trans. R. Soc. London. Ser. A Math. Phys. Sci.* **1948**, *240*, 599–642. [CrossRef]
41. Zélis, P.M.; Pasquevich, G.A.; Stewart, S.J.; van Raap, M.B.F.; Aphesteguy, J.; Bruvera, I.J.; Laborde, C.; Pianciola, B.; Jacobo, S.; Sánchez, F.H. Structural and Magnetic Study of Zinc-Doped Magnetite Nanoparticles and Ferrofluids for Hyperthermia Applications. *J. Phys. D. Appl. Phys.* **2013**, *46*, 125006. [CrossRef]
42. Usov, N.A.; Nesmeyanov, M.S.; Gubanova, E.M.; Epshtein, N.B. Heating Ability of Magnetic Nanoparticles with Cubic and Combined Anisotropy. *Beilstein J. Nanotechnol.* **2019**, *10*, 305–314. [CrossRef] [PubMed]
43. Martinez-Boubeta, C.; Simeonidis, K.; Serantes, D.; Conde-Leborán, I.; Kazakis, I.; Stefanou, G.; Peña, L.; Galceran, R.; Balcells, L.; Monty, C.; et al. Adjustable Hyperthermia Response of Self-Assembled Ferromagnetic Fe-MgO Core-Shell Nanoparticles by Tuning Dipole-Dipole Interactions. *Adv. Funct. Mater.* **2012**, *22*, 3737–3744. [CrossRef]
44. Ovejero, J.G.; Cabrera, D.; Carrey, J.; Valdivielso, T.; Salas, G.; Teran, F.J. Effects of Inter- and Intra-Aggregate Magnetic Dipolar Interactions on the Magnetic Heating Efficiency of Iron Oxide Nanoparticles. *Phys. Chem. Chem. Phys.* **2016**, *18*, 10954–10963. [CrossRef] [PubMed]
45. Landi, G.T. Role of Dipolar Interaction in Magnetic Hyperthermia. *Phys. Rev. B-Condens. Matter Mater. Phys.* **2014**, *89*, 014403. [CrossRef]
46. Maniotis, N.; Gitsou, M.; Maragakis, M. Conjugating Magnetic Nanoparticles Anisotropy to Their Dipolar Interactions: Effect on the Hyperthermic Losses Index via Micromagnetic Simulations. *J. Magn. Magn. Mater.* **2025**, *617*, 172843. [CrossRef]
47. Barrera, G.; Allia, P.; Tiberto, P. Dipolar Interactions among Magnetite Nanoparticles for Magnetic Hyperthermia: A Rate-Equation Approach. *Nanoscale* **2021**, *13*, 4103–4121. [CrossRef] [PubMed]

48. Vamvakidis, K.; Maniotis, N.; Dendrinou-Samara, C. Magneto-Fluorescent Nanocomposites: Experimental and Theoretical Linkage for the Optimization of Magnetic Hyperthermia. *Nanoscale* **2021**, *13*, 6426–6438. [CrossRef] [PubMed]
49. Myrovali, E.; Maniotis, N.; Makridis, A.; Terzopoulou, A.; Ntomprougkidis, V.; Simeonidis, K.; Sakellari, D.; Kalogirou, O.; Samaras, T.; Salikhov, R.; et al. Arrangement at the Nanoscale: Effect on Magnetic Particle Hyperthermia. *Sci. Rep.* **2016**, *6*, 37934. [CrossRef] [PubMed]
50. Abbasi Aval, N.; Pirayesh Islamian, J.; Hatamian, M.; Arabfirouzjaei, M.; Javadpour, J.; Rashidi, M.R. Doxorubicin Loaded Large-Pore Mesoporous Hydroxyapatite Coated Superparamagnetic Fe_3O_4 nanoparticles for Cancer Treatment. *Int. J. Pharm.* **2016**, *509*, 159–167. [CrossRef] [PubMed]
51. Usov, N.A.; Grebenshchikov, Y.B. Hysteresis Loops of an Assembly of Superparamagnetic Nanoparticles with Uniaxial Anisotropy. *J. Appl. Phys.* **2009**, *106*, 023917. [CrossRef]
52. Tan, R.P.; Carrey, J.; Respaud, M. Magnetic Hyperthermia Properties of Nanoparticles inside Lysosomes Using Kinetic Monte Carlo Simulations: Influence of Key Parameters and Dipolar Interactions, and Evidence for Strong Spatial Variation of Heating Power. *Phys. Rev. B-Condens. Matter Mater. Phys.* **2014**, *90*, 214421. [CrossRef]
53. Guimarães, A.P. *Principles of Nanomagnetism*; Springer: Cham, Switzerland, 2009; ISBN 978-3-642-01481-9.
54. Suriyanto; Ng, E.Y.K.; Kumar, S.D. Physical Mechanism and Modeling of Heat Generation and Transfer in Magnetic Fluid Hyperthermia through Néelian and Brownian Relaxation: A Review. *Biomed. Eng. Online* **2017**, *16*, 36. [CrossRef] [PubMed]
55. Iacovita, C.; Stiufiuc, G.F.; Dudric, R.; Vedeanu, N.; Tetean, R.; Stiufiuc, R.I.; Lucaciu, C.M. Saturation of Specific Absorption Rate for Soft and Hard Spinel Ferrite Nanoparticles Synthesized by Polyol Process. *Magnetochemistry* **2020**, *6*, 23. [CrossRef]
56. McGhie, A.A.; Marquina, C.; O'Grady, K.; Vallejo-Fernandez, G. Measurement of the Distribution of Anisotropy Constants in Magnetic Nanoparticles for Hyperthermia Applications. *J. Phys. D Appl. Phys.* **2017**, *50*, 455003. [CrossRef]
57. Mehdaoui, B.; Meffre, A.; Lacroix, L.M.; Carrey, J.; Lachaize, S.; Gougeon, M.; Respaud, M.; Chaudret, B. Large Specific Absorption Rates in the Magnetic Hyperthermia Properties of Metallic Iron Nanocubes. *J. Magn. Magn. Mater.* **2010**, *322*, L49–L52. [CrossRef]
58. Faílde, D.; Ocampo-Zalvide, V.; Serantes, D.; Iglesias, Ò. Understanding Magnetic Hyperthermia Performance within the "Brezovich Criterion": Beyond the Uniaxial Anisotropy Description. *Nanoscale* **2024**, *16*, 14319–14329. [CrossRef] [PubMed]
59. Hergt, R.; Hiergeist, R.; Hilger, I.; Kaiser, W.A.; Lapatnikov, Y.; Margel, S.; Richter, U. Maghemite Nanoparticles with Very High AC-Losses for Application in RF-Magnetic Hyperthermia. *J. Magn. Magn. Mater.* **2004**, *270*, 345–357. [CrossRef]
60. Darwish, M.S.A.; Kim, H.; Lee, H.; Ryu, C.; Lee, J.Y.; Yoon, J. Synthesis of Magnetic Ferrite Nanoparticles with High Hyperthermia Performance via a Controlled Co-Precipitation Method. *Nanomaterials* **2019**, *9*, 1176. [CrossRef] [PubMed]
61. Kim, J.-W.; Wang, J.; Kim, H.; Bae, S. Concentration-Dependent Oscillation of Specific Loss Power in Magnetic Nanofluid Hyperthermia. *Sci. Rep.* **2021**, *11*, 733. [CrossRef] [PubMed]

Disclaimer/Publisher's Note: The statements, opinions and data contained in all publications are solely those of the individual author(s) and contributor(s) and not of MDPI and/or the editor(s). MDPI and/or the editor(s) disclaim responsibility for any injury to people or property resulting from any ideas, methods, instructions or products referred to in the content.